AD NUMBER
ADC026872
CLASSIFICATION CHANGES
TO: unclassified
FROM: confidential
LIMITATION CHANGES
TO: Approved for public release, distribution unlimited
FROM: Controlling DoD Organization. Naval Electronic Systems Command, Washington, DC 20360.
AUTHORITY
ONR ltr, 31 Jan 2006; ONR ltr, 31 Jan 2006

CONFIDENTIAL

NOSC

NOSC TR 703

LEVEL II

NOSC TR 703

Technical Report 703

NORMAL MODE ANALYSIS OF PROPAGATION LOSS AT THE BEARING STAKE SITES (U)

DF Gordon

August 1981

Final report: October 1980 — August 1981

Prepared for
Naval Electronic Systems Command

Classified by: OPNAVINST S5513.5-03
Review on: 8 October 1994

NAVAL OCEAN SYSTEMS CENTER
SAN DIEGO, CALIFORNIA 92152

CONFIDENTIAL

NAVAL OCEAN SYSTEMS CENTER, SAN DIEGO, CA 92152

AN ACTIVITY OF THE NAVAL MATERIAL COMMAND

SL GUILLE, CAPT, USN
Commander

HL BLOOD
Technical Director

ADMINISTRATIVE INFORMATION (U)

(U) The work reported herein was conducted for the Naval Electronic Systems Command under PE 62759, XF-59-552, over the period October 1980 – August 1981.

Released by
MR Akers, Head
Systems Concepts and
Analysis Division

Under authority of
EB Tunstall, Head
Surveillance Systems
Department

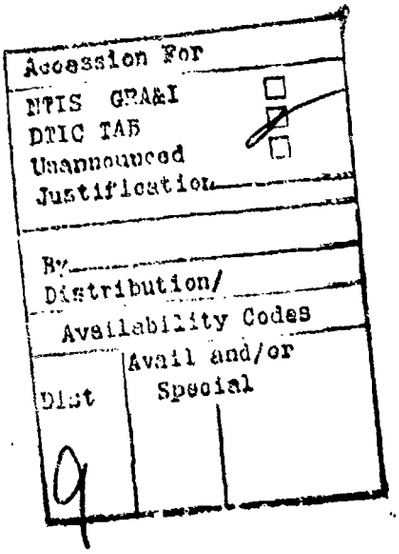

UNCLASSIFIED

SECURITY CLASSIFICATION OF THIS PAGE (When Data Entered)

CONFIDENTIAL
(This page is unclassified)

REPORT DOCUMENTATION PAGE	READ INSTRUCTIONS BEFORE COMPLETING FORM
1. REPORT NUMBER: NOSC Technical Report 703 (TR 703)	2. GOVT ACCESSION NO.: AD-C026 872 / 3. RECIPIENT'S CATALOG NUMBER:
4. TITLE (and Subtitle): NORMAL MODE ANALYSIS OF PROPAGATION LOSS AT THE BEARING STAKE SITES (U)	5. TYPE OF REPORT & PERIOD COVERED: Final Report: October 1980 – August 1981
	6. PERFORMING ORG. REPORT NUMBER:
7. AUTHOR(s): DF Gordon	8. CONTRACT OR GRANT NUMBER(s):
9. PERFORMING ORGANIZATION NAME AND ADDRESS: Naval Ocean Systems Center, San Diego, CA 92152	10. PROGRAM ELEMENT, PROJECT, TASK AREA & WORK UNIT NUMBERS: 62759, XF-59-552
11. CONTROLLING OFFICE NAME AND ADDRESS: Naval Electronic Systems Command, Washington, DC 20360	12. REPORT DATE: August 1981
	13. NUMBER OF PAGES: 60
14. MONITORING AGENCY NAME & ADDRESS (if different from Controlling Office)	15. SECURITY CLASS. (of this report): Confidential
	15a. DECLASSIFICATION/DOWNGRADING SCHEDULE: Review on 8 October 1994
16. DISTRIBUTION STATEMENT (of this Report)	
17. DISTRIBUTION STATEMENT (of the abstract entered in Block 20, if different from Report)	
18. SUPPLEMENTARY NOTES	
19. KEY WORDS (Continue on reverse side if necessary and identify by block number): Underwater acoustics; Bearing Stake; Propagation loss; Sea floor reflection	
20. ABSTRACT (Continue on reverse side if necessary and identify by block number): Propagation loss data for the bottom-limited sites of the Bearing Stake exercise are analyzed and values derived for attenuation at low frequency. A discrepancy is revealed between measured attenuation and that computed on the basis of observed sediment parameters.	

DD FORM 1 JAN 73 1473 EDITION OF 1 NOV 65 IS OBSOLETE

S/N 0102-LF-014-6601

UNCLASSIFIED 31159

SECURITY CLASSIFICATION OF THIS PAGE (When Data Entered)

CONFIDENTIAL
(This page is unclassified)

S/N 0102- LF- 014- 6601

SUMMARY (U)

OBJECTIVE (U)

(C) Analyze propagation loss observed at the bottom-limited sites of the Bearing Stake exercise. Determine the effectiveness of computer modeling of propagation loss using environmental parameters derived from the Bearing Stake exercise. Predict acoustic propagation in seasons other than those of the Bearing Stake exercises. Determine near-bottom and near-surface propagation effects that can influence sensor depth selection.

RESULTS (U)

1. (C) Very low bottom losses at the Bearing Stake sites cause very low attenuation in long-range sound propagation. Values for attenuation from 0.001 to 0.004 dB/km were observed at 25 Hz.

2. (C) Computations using sediment models prepared from Bearing Stake observations give attenuations from 0.005 to 0.01 dB/km at 25 Hz. These are two to four times larger than the observed values even though sediment attenuations have already been adjusted downward to match the low losses.

3. (U) The source strength at 25 Hz used in the Bearing Stake exercise was 1.5 to 2 dB higher than previously estimated.

4. (U) Seasonal changes result in less than 2 dB difference in average propagation loss to 750 km range at 25 Hz. At 140 Hz, seasonal differences can be up to 19 dB.

5. (U) A near-bottom maximum or notch in propagation loss occurs at all the bottom-limited sites. This notch results from destructive interference between multipaths.

6. (U) Arrays suspended above the bottom can gain up to 3 dB in signal-to-noise over arrays on the ocean bottom. However, the optimum distance above the bottom depends on frequency, site, and season.

7. (U) At Site 5, a 100-m-deep source is not bottom limited in some seasons.

8. (U) Sediment sound speeds slower than the water sound speed produce more complicated reflection loss functions than do fast bottoms.

9. (U) At the Bearing Stake sites there is no clear correlation between season of the year and sound speed at 100 m depth.

APPLICATION TO NAVY PROBLEMS (U)

1. (C) Average propagation loss at the Bearing Stake sites is tabulated in terms of two parameters, H_0 and α, for three frequencies between 25 and 290 Hz.

2. (U) Seasonal bounds on these two parameters have been determined.

3. (U) Detailed propagation plots near the surface and bottom can aid sensor depth placement.

RECOMMENDATIONS (U)

1. (U) Investigate reasons for discrepancy between attenuation as observed and as computed from observed sediment parameters.

2. (U) Analyze propagation at Site 4, which is not bottom limited.

CONTENTS (U)

ILLUSTRATIONS (U)

ILLUSTRATIONS (Continued) (U)

ILLUSTRATIONS (Continued) (U)

TABLES (U)

INTRODUCTION (U)

(C) The Bearing Stake exercise was a major acoustic survey program conducted in the Northwest Indian Ocean from January through May 1977. The program was sponsored by the Naval Electronic Systems Command (PME-124). A bottom-mounted array was deployed at each of five sites indicated in Fig 1. An acoustic data capsule (ACODAC) was usually also deployed at each site. Projector tows or shot runs were made along paths marked on the figure.

(C) Propagation loss measured to selected hydrophones of the bottom-mounted array and ACODAC has been analyzed and is reported in Ref 1. Computer modeling of the propagation loss at Site 1 was used as an aid in analyzing the data and to examine effects not available from the experimental setup. In this report, the comparison between modeled and observed data is extended to Sites 3 and 5. The data for Site 2 are of questionable quality. This is apparently due to bathymetry at and near the receiving hydrophones. Such effects cannot be addressed by the computer program used here, so no modeling of Site 2 was attempted.

(C) Propagation at Site 4, in deeper water, is via a mixture of convergence zone and bottom-reflected paths. It thus differs from the other four sites, where prepagation is via bottom-reflected paths only. For this reason, propagation at Site 4 is a separate topic and will be addressed in a future report.

(C) Three aspects of propagation are treated in this report. First, the propagation is analyzed by subtracting the 10 log (r) spreading loss and comparing the remaining average loss levels and attenuation rates. This technique characterizes the unique sound transmission properties of this area of the Indian Ocean. Because these properties depend upon the bottom reflection effects, an analysis of bottom reflection is presented. Second, the computer modeling is extended to different seasons to determine the yearly variability of the propagation loss. Third, near-bottom effects are studied to determine if they can be used to gain signal-to-noise advantages by selecting near-bottom array depths.

(U) Normal mode modeling has also been used to analyze towed array performance at the Bearing Stake sites. This project is reported in Ref 2.

PROPAGATION LOSS (U)

COMPUTER MODELING (U)

(U) Propagation loss is computed using a normal mode program. This program gives a wave theory solution to a boundary value problem in which the sound speed profile is constant with range. The bottom is flat and is modeled as additional fluid layers with characteristic sound speed, density, and sound attenuation. The program is described in Ref 3.

---

1. NOSC Technical Report 467, "Propagation Loss Assessment of the Bearing Stake Exercise (U)," M.A. Pedersen and G.S. Yee, Sept 1979. (CONFIDENTIAL)

2. NOSC Technical Report 564, "Array Simulation at the Bearing Stake Sites (U)," D.F. Gordon, April 1981. (CONFIDENTIAL)

3. NOSC Technical Report 393, "Underwater Sound Propagation Loss Program, Computation by Normal Modes of Layered Oceans and Sediments," D.F. Gordon, May 1979.

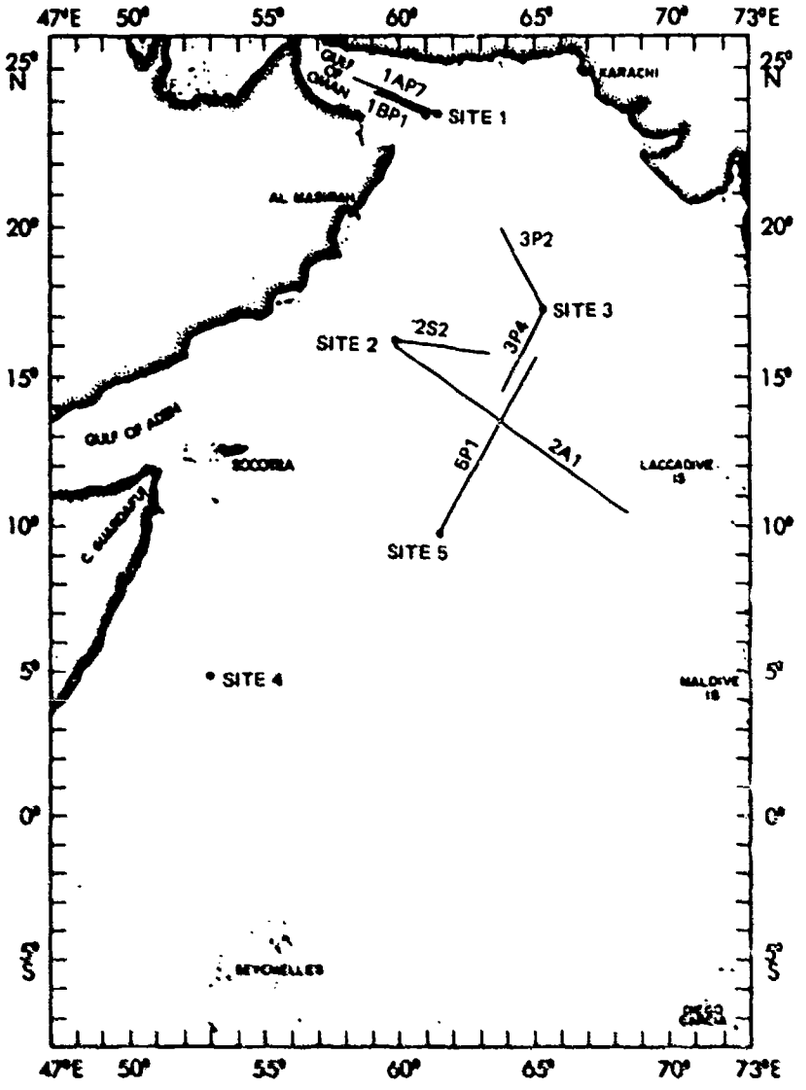

(CONFIDENTIAL)

(U) Figure 1. Map showing the location of the Bearing Stake sites and tows or shot runs reported here.

(U) Reference 4 gives the representative sound speed profiles that were derived from measurements taken during the exercise. Reference 5 gives the sediment structure and properties derived from both direct measurements and analysis of acoustic reflection measurements. The normal mode program is limited to 12 layers for modeling the sound speed

4. NORDA Report 18, "Bearing Stake Exercise Sound Speed and Other Environmental Variability (U)," D.F. Fenner and W.J. Cronin, Jr., Sept 1978. (CONFIDENTIAL)

5. ARL-TR-79-24, "Analysis of Acoustic Bottom Interaction in Bearing Stake (U)," S.K. Mitchell and others, Feb 1979. (CONFIDENTIAL)

profile in both the water and sediment. Therefore, judgement must be used to model the most important features of both. Figure 2 shows the three representative profiles used and the layers used to represent them in the computer program. The layers in the sediment are shown in a later section on reflection losses.

(U) The normal mode program is also limited to 250 modes. This is not an absolute limit, but it is economically wise to stay within it. Bottom loss propagation requires many modes because high grazing angles correspond to high mode members. At the highest frequency used here, 290 Hz, the 250 modes were barely sufficient, and losses for ranges up to 100 km can be off a little. Where spot checks indicated this error to be greater than 0.1 dB, extra sets of modes were run and combined by hand to correct the errors.

(C) Table 1 gives the experimental parameters for the particular runs reported here. The same parameters were used for the normal mode runs except as noted in the table. The first number of the run designations in the table is the site number. Site 1 was occupied

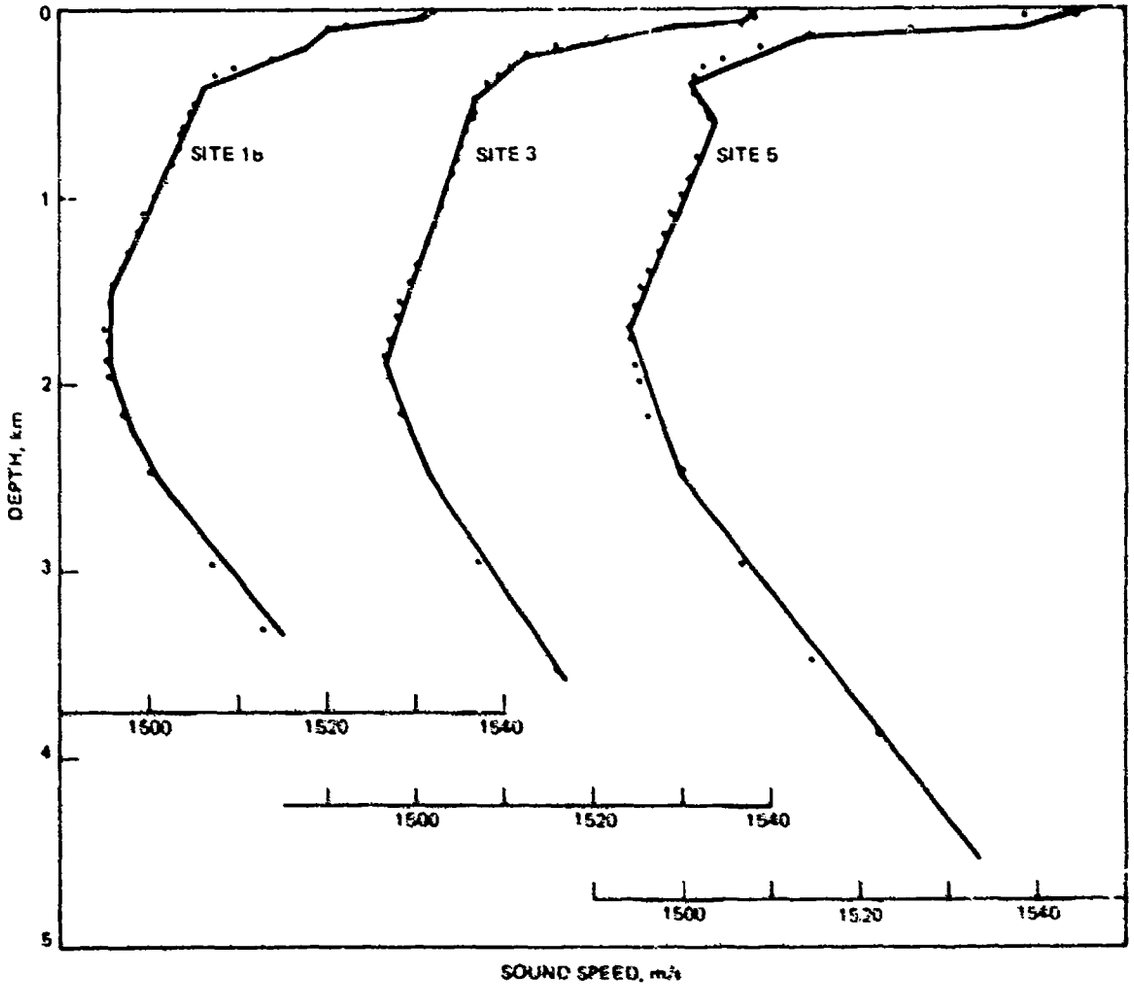

(UNCLASSIFIED)

(U) Figure 2. Sound speed profiles showing the layers used in the normal mode computations.

Run Designation	Frequency, Hz	Source Depth, m	Receiver Depth, m	Maximum Range, km
1AP7	25	84	3350	200
1AP7	140	18	3350	200
1AP7	290	18	3350	200
1BP1	25	102	3350	298
1BP1	140	18	3350	298
1BP1	290	18	3350	298
2A1	20	91	3162	1093
2S2	140	18	3162	372
2A1	300	18	3162	1093
3P4	25	77	3546	352
3P4	140	18	3546	352
3P4	290	18	3546	352
3P2	290	18	3546	333
5P1	22	77	3844*	759
5P1	140	18	3844*	759
5P1	290	18	3844*	759

*Receiver depth of 4534 m was used in normal mode computations.

(CONFIDENTIAL)

(U) Table 1. Experimental parameters for selected Bearing Stake CW source tows and bomb runs.

twice during the exercises, leading to designations 1A and 1B. Normal mode parameters were selected to match Site 1B source depth. The letter following the site designation stands for a projector tow (P) or a shot run made by a ship (S) or by an airplane (A). The final number denotes the particular event at that site.

(U) At Site 5, the receivers were on a small hill overlooking the alluvial fan. To intercompare modeled results of the three sites, the receiver for Site 5 was modeled as though it were on the flat bottom of the fan. When comparing the modeled results with observed data, this change in receiver depth will make less than 1 dB difference in the average propagation loss. A much larger difference occurs because the hill shadows many ray paths to the receiver. This effect cannot be modeled with the normal mode program, and corrections for it will be discussed when the losses are compared in a later section of this report. Because the uncertainty due to this shadowing effect is large, the discrepancy between actual and modeled receiver depth was felt to be permissible.

(U) The receiver at Site 2 was also in a hilly area. This probably caused some anomalies in the propagation there as discussed earlier. The receivers at Sites 1A, 1B, and 3 are on the flat ocean bottom.

DATA REDUCTION (U)

(U) Bearing Stake propagation loss in the bottom-limited areas is characterized by large variability but small propagation losses. These properties arise from very low bottom

reflection losses and the many multipaths that result. The variability has been investigated in detail and will be reported in Ref 6. The amplitude distributions of large quantities of both observed and modeled data are reported there. Those data were also available to this work as average sound intensities in 50-km bins, so they served as a starting point and as a framework for this investigation of propagation loss.

(C) Range bins are centered on each even 50 km. The first bin extends from 25 to 75 km, the second from 75 to 125 km, etc. Some of the shortest propagation runs in Site 1 extend to less than 225 km and thus yield three range bins. The longest at Site 2 was used to 875 km, giving 17 range bins.

(U) Where additional computed data were needed, random phase mode sums were used. Adding modes in random phase is a simple and effective way to obtain propagation losses equivalent to those averaged in range. Such random phase losses are constrained to lie on a smooth curve, increasing with range. For these reasons we chose to use random phase computations to investigate the widest range of cases. Figure 3 is a comparison of average normal mode losses as computed by the two methods. Note the smoothness of the random phase losses and the variation in the 50-km bin averages. With 5000 points per bin in this case, the variation of up to 0.5 dB in the averages is not likely to be due to chance

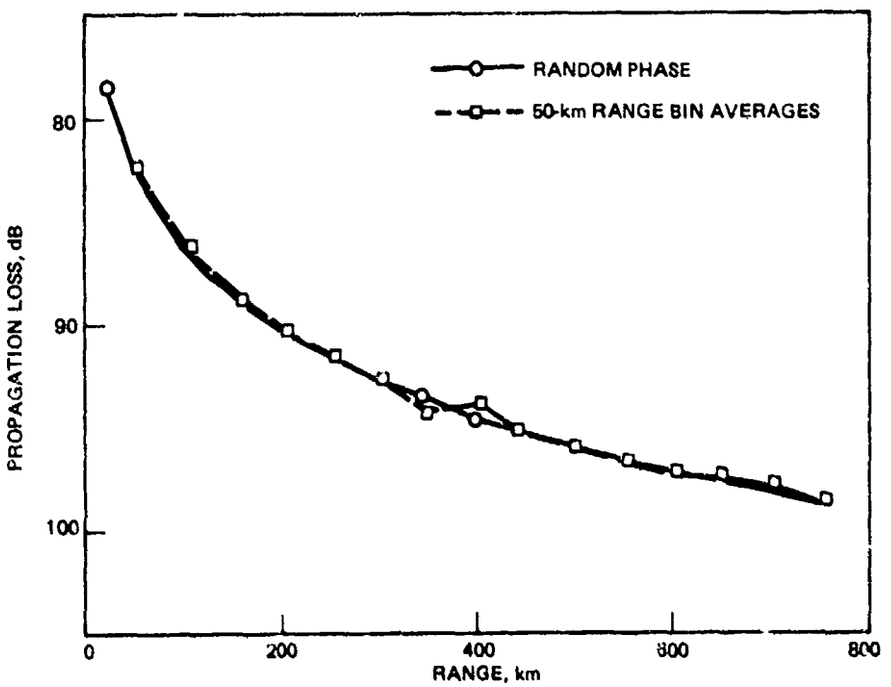

(UNCLASSIFIED)

(U) Figure 3. Comparison of normal mode propagation losses computed by random phase mode addition and computed by phased mode addition and then averaged.

6. M.A. Pedersen, et al, "Comparison of Theoretical and Experimental Statistical Distributions of Bearing Stake Propagation Loss" (NOSC TR in preparation).

summing of random values. Rather, intervals of constructive or destructive mode phase addition are probably long enough to occupy a significant part of a 50-km range bin, so that many fewer than 5000 random range intervals occur in a range bin. This accounts for the variability from bin to bin.

(U) With a single propagation loss in decibels for each bin, our technique is to remove the cylindrical spreading term and make a linear least squares fit (or linear regression) to the constant H_o and the slope α. That is, we assume the following propagation loss dependence.

$$H(r) = H_o + 10 \log (r) + \alpha r \tag{1}$$

where H is the propagation loss in decibels, r is range in kilometers, and α is the attenuation rate. In the regression, H_o and α are determined by making a linear fit to y, where

$$y = H(r) - 10 \log (r) = H_o + \alpha r \tag{2}$$

with r as the dependent variable. The overall propagation loss of two propagation runs can be compared by comparing the two values of H_o. The antilog of $H_o/10$ gives the transition range where spherical spreading gives way to cylindrical spreading. The damping term α measures losses in excess of cylindrical spreading which are predominantly bottom reflection losses.

(U) We give three standard errors with the tabulated results: $s_{y|r}$, s_H, and s_α. The standard error of estimate $s_{y|r}$ gives the variation of the given points about the regression line. It is given by

$$s_{y|r}^2 = (n-1)(s_y^2 - \alpha^2 s_r^2)/(n-2) \tag{3}$$

where n is the number of points (range bins) in the run, and s_y and s_r, are the standard deviations of y and r. The variation of the zero range intercept H_o is given by

$$s_H^2 = s_{y|r}^2 \left[1/n + \bar{r}^2/s_r^2 (n-1) \right] . \tag{4}$$

The variation in α is given by

$$s_\alpha^2 = s_{y|r}^2/s_r^2 (n-1) . \tag{5}$$

These are estimates of the population standard errors and, assuming the sample points are taken from a normally distributed population, they can be used in t-tests for significance or testing hypotheses about the regression parameters.

(U) In the following tabulations, when H_o or α are given, they will be listed with their standard error, eg, 35.56 ± 1.03 dB. This means that, if normally distributed, 68 percent of the observations of H_o will fall within 1.03 dB of the true value.

(U) When the intensities are averaged in a range bin, it is reasonable to assign the average to the midpoint of the bin. However, when fitting to a cylindrical spreading curve, a better fit is obtained if the average point of an interval is assigned to the range of the average value of a cylindrical function, over the range bin. The average is

$$(b-a)^{-1}\int_a^b dr/r = (\log b - \log a)/(b-a) \qquad (6)$$

The reciprocal of this average gives the range required. Table 2 gives the centers of the 50-km range bins and also the modified centers from Eq (6). The differences are largest at short ranges, where the curvature of the cylindrical spreading curve is greatest. For all data sets used, the standard error of estimate is smaller when using the modified bin ranges than when using the midpoints, so reported results are for the modified ranges. Points determined by random phase mode addition correspond to averages at a point and not over an interval, so such points do not need to be shifted.

(U) The assumption that y in Eq (2) is linear is an approximation, particularly for bottom-reflected propagation. However, it does not seem to be a serious error, as indicated by the following argument. Figure 4 shows a typical case, with both observed data and normal mode random phase results for Site 5, 140 Hz. A least squares fit to both sets is shown. The normal mode propagation loss data, a random phase sum, are expected to lie on a smooth curve. From the figure it can be seen that this curve is not quite a straight line. This is because the loss is a sum of modes with different attenuation rates, and at longer ranges the modes of larger attenuation have been stripped out. Physically, this corresponds to higher angle bottom reflected paths being stripped out due to larger bottom losses per reflection and to more frequent reflections.

(U) The slope of the normal mode line in Fig 4 is 0.0198 dB/km. A second-degree polynomial fit (adding r^2 as a variable) fits the points more closely and gives a slope at 50 km of 0.022 dB/km and at 750 km of 0.017 dB/km.

(U) We thus see that the slope α is the attenuation rate at about the midrange of the given data, about 400 km when data are given to 750 km. When observed data are given for only a few range bins at short range, a somewhat high value of α will be obtained. However, the scatter of the observed data is too great to be sensitive to these small differences in slope. Therefore, in the remainder of this report, we will assume the linear model is acceptable and will compare runs on the basis of H_o and α. In Fig 4 it is apparent the α for the two runs is different. H_o may well be the same.

Center, km	Range of average, km
50	45.512
100	97.881
150	148.601
200	198.954
300	299.304
500	499.583
700	699.703

(UNCLASSIFIED)

(U) Table 2. The centers of some 50-km range bins and the range of the average value of 1/r for the same range bins.

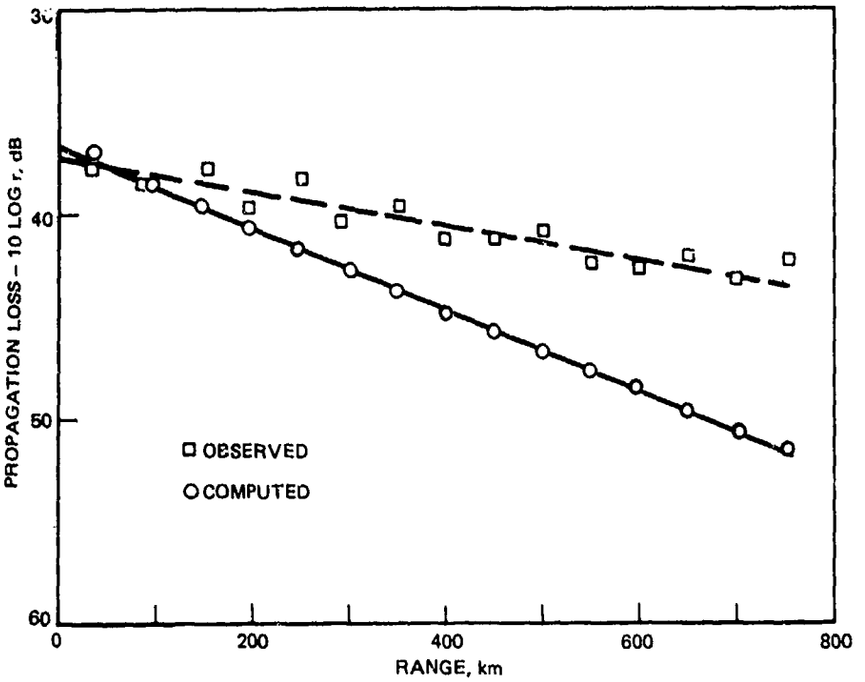

(CONFIDENTIAL)

(U) Figure 4. Propagation loss with 10 log(r) removed and least squares fits for Site 5, 140 Hz. Observed data averaged in 50-km bins. Computed data are by random phase mode addition.

(U) Table 3 gives the regression parameters for the observed and for the computed data. The runs labeled "NMRP" are normal mode and random phase mode addition. Other results are for points from each 50-km range bin. Thus, the first result for Site 1A, labeled "data," where n is three for an observed propagation run, tow P7, which gave data for three range bins covering a range from 25 to 175 km. The third entry in the table, labeled "NM," is for normal mode intensities computed every 10 m in range, averaged over 50-km range bins from 25 to 775 km, giving 15 points. Other entries in Table 3 will be described later.

ANALYSIS OF OBSERVED DATA (U)

(U) Reference 1 picks out and tabulates propagation losses (50-km bin averages) for the best propagation loss runs at each site for low, medium, and high frequency, usually 25, 140, and 290 Hz. These tabulations are on pages 76, 108, 125, and 169 of Ref 1. The reason for selecting these runs is the assumption that these best runs suffer little shadowing from nearby bottom features and should best correspond to theoretical propagation along unobstructed paths. For this reason, these particular runs are used here as representative of each site and are the observed data tabulated in Table 3. Values of H_o and α for these data from Table 3 will be discussed next.

(U) The values of H_o for the three frequency groups are plotted in Fig 5. Two "best" runs were given for Site 3 at 290 Hz in Ref 1, and both are plotted on the figure. The right-hand scale on the figure gives the transition range, R_o, the range at which spherical spreading changes to cylindrical spreading. It is approximated by

$$10 \log R_o = H_o \qquad (7)$$

LOW FREQUENCY

Site	Type	H_o, dB	α, dB/km	Standard Error of Estimate, dB	Frequency Hz	n,
1AP7	DATA	32.32 ± 0.002	- 0.0023 ± 0.0000	0.0014	25	3
1BP1	DATA	30.98 ± 0.37	0.0017 ± 0.0022	0.3566	25	5
1	NM	33.19 ± 0.24	0.0100 ± 0.0005	0.4459	25	15
1	NMRP	33.00 ± 0.16	0.0103 ± 0.0004	0.2978	25	15
1MAX	NMRP	33.85 ± 0.19	0.0151 ± 0.0004	0.3589	25	15
1MIN	NMRP	34.10 ± 0.18	0.0120 ± 0.0004	0.3345	25	15
2A1	DATA	32.28 ± 1.95	0.0073 ± 0.0006	0.6448	25	17
3P4	DATA	32.03 ± 1.02	- 0.0035 ± 0.0053	1.1143	25	6
3	NM	33.52 ± 0.10	0.0080 ± 0.0002	0.1893	25	15
3	NMRP	33.08 ± 0.15	0.0087 ± 0.0003	0.2695	25	15
3MAX	NMRP	33.13 ± 0.14	0.0094 ± 0.0003	0.2601	25	15
3MIN	NMRP	32.79 ± 0.14	0.0079 ± 0.0003	0.3594	25	15
5PI	DATA	33.07 ± 0.36	0.0011 ± 0.0008	0.6567	22	15
5	NM	33.89 ± 0.09	0.0046 ± 0.0002	0.1579	22	15
5	NMRP	33.73 ± 0.14	0.0049 ± 0.0003	0.2602	22	15
5MAX	NMRP	33.66 ± 0.15	0.0053 ± 0.0003	0.2759	22	15
5MIN	NMRP	33.52 ± 0.14	0.0048 ± 0.0003	0.2611	22	15

MEDIUM FREQUENCY

1AP7	DATA	38.33 ± 1.77	0.0017 ± 0.0167	1.2185	140	3
1BP1	DATA	33.76 ± 1.07	0.0234 ± 0.0065	1.0487	140	5
1	NMRP	39.33 ± 0.63	0.0481 ± 0.0013	1.1568	140	15
1MAX	NMRP	41.22 ± 0.56	0.0551 ± 0.0012	1.0358	140	15
1MIN	NMRP	41.01 ± 0.61	0.0465 ± 0.0013	1.1206	140	15
2S2	DATA	42.78 ± 3.50	- 0.0014 ± .0146	3.07	140	6
3P4	DATA	35.91 ± 1.27	0.0150 ± 0.0065	1.3846	140	6
3	NM	37.16 ± 0.54	0.0498 ± 0.0002	0.4340	140	15
3	NMRP	37.46 ± 0.32	0.0432 ± 0.0007	0.5810	140	15
3MAX	NMRP	37.31 ± 0.32	0.0457 ± 0.0007	0.5885	140	15
3MIN	NMRP	37.90 ± 0.45	0.0365 ± 0.0002	0.8333	140	15
5PI	DATA	37.25 ± 0.41	0.0083 ± 0.0009	0.7649	140	15
5	NMRP	36.76 ± 0.08	0.0198 ± 0.0002	0.1546	140	15
5MAX	NMRP	36.67 ± 0.11	0.0199 ± 0.0002	0.1948	140	15
5MIN	NMRP	37.22 ± 0.11	0.0189 ± 0.0002	0.1996	140	15

(CONFIDENTIAL)

(U) Table 3. Fits of $H(r) = 10 \log(r) + H_o + \alpha r$ to the averages of 50-km range bins or random phase mode sums at 50-km range intervals. Standard errors are included.

HIGH FREQUENCY

Site	Type	H_o, dB	α, dB/km	Standard Error of Estimate, dB	Frequency n, Hz	
1AP7	DATA	34.00 ± 0.48	0.0472 ± 0.0045	0.3306	290	3
1BP1	DATA	36.92 ± 0.80	0.0334 ± 0.0049	0.7800	290	5
1	NMRP	39.63 ± 0.32	0.1025 ± 0.0007	0.5942	290	15
2A1	DATA	41.75 ± 1.02	0.0212 ± 0.0018	1.851	300	17
3P4	DATA	37.46 ± 0.97	0.0347 ± 0.0050	1.0641	290	6
3P2	DATA	35.06 ± 0.98	0.0456 ± 0.0051	1.0754	290	6
3	NMRP	37.73 ± 0.26	0.0727 ± 0.0002	0.4743	290	15
5P1	DATA	38.72 ± 0.64	0.0177 ± 0.0014	1.1780	290	15
5	NMRP	38.82 ± 0.22	0.0395 ± 0.0005	0.4090	290	15

(CONFIDENTIAL)

(U) Table 3, continued.

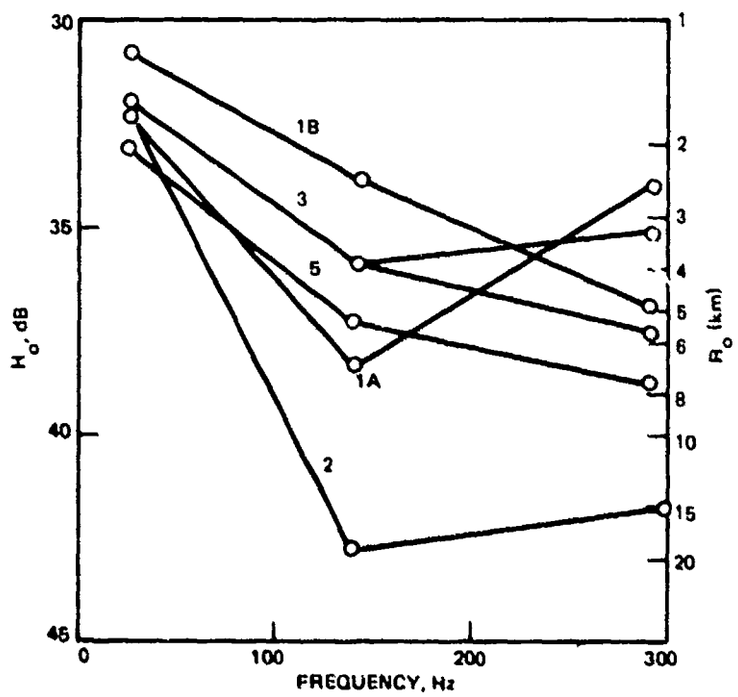

(CONFIDENTIAL)

(U) Figure 5. Zero intercept of least squares fits to loss – 10 log (r) for the observed data. Range of change from spherical to cylindrical spreading is given on right-hand scale.

This concept is an approximation, as was the linearity of y; but in general, shallower depths and lower reflection losses should give smaller values of R_O. In general, Site 1 (1A and 1B) has the shallowest depth but greatest bottom loss, while Site 5 has the greatest depth but least loss. Therefore, it is not surprising that Fig 5 does not show a clear-cut dependence on site. An analysis of variance using site and frequency does not indicate at the 5-percent significance level that site affects H_O. Certain effects on H_O due to such things as source level and the contours of the bottom at the hydrophones will be discussed when comparison is made with normal mode results.

(U) The analysis of variance indicates that frequency is a significant variable at the 5-percent level. Figure 5 shows, however, that the significant frequency dependence is between 25 Hz and the higher frequencies. There is no clear increase in H_O from 140 to 290 Hz.

(U) We can therefore conclude that at 25 Hz, the spreading of energy has become cylindrical, or reached R_O, by a range of 2 km. At the two higher frequencies, R_O tends to be several times greater. R_O is probably the range at which the bottom-reflected field becomes comparable in intensity to the direct field. In all cases our first data points at 20 km are well beyond R_O. If this were not so, they might unduly elevate the fitted line and increase its slope.

(U) The other parameter, the attenuation α, is plotted in Fig 6. Here again an analysis of variance indicates that α depends on frequency but not on site at the 5-percent significance level. Thus, as is obvious from Fig 6, α increases with frequency, but there is too much variation to say that a high value of α at one frequency implies a high value for the same site at another frequency. Therefore, from these data we cannot correlate α with the physical properties of the sediments at the different sites.

(C) The attenuation does increase with frequency, and a line through the average α at each of the three frequencies is roughly linear. In this frequency range we can say that attenuation increases by the slope of this line, or 0.01 dB/km per 100 Hz. Thorp's attenuation (Ref 7) accounts for about one-third of α at 290 Hz. Should the linear trend in α continue, Thorp's curve would cross it near 9 kHz. However, there is little justification for extending the linear curve beyond a few hundred hertz or for assuming Thorp's curve is valid in the Indian Ocean. We therefore can only conclude that, in the frequency range of our data, bottom loss is the principal loss mechanism and increases with frequency in a near-linear fashion.

(U) Three values of α are negative. These are Sites 1A and 3 at 25 Hz and Site 2 at 140 Hz. In the last two, α is within one standard deviation of zero, so we can assume that α should have had a positive value. At Site 1A, only three data bins are given. These three points by chance fell near a straight line, giving an estimate of the standard deviation that is almost certainly too small. This is suggested by the standard error, which is less than 1 percent of the next larger standard error in Table 3.

(U) It is not likely that a true negative α was observed because propagation runs usually were directly towards or away from the hydrophone sites, which doesn't permit long-range paths to be distinct from short-range paths over their entire length. However, effects which could produce a negative α include change in water depth, which can affect mode strength and mode coupling (as in surface decoupling), changes in sound speed profile, which affect ducting, and even focusing in the horizontal plane due to bathymetry.

---

7. W.H. Thorp, "Analytic Description of the Low-Frequency Attenuation Coefficient," J. Acoust. Soc. Am., 42:1, p 270, July 1967.

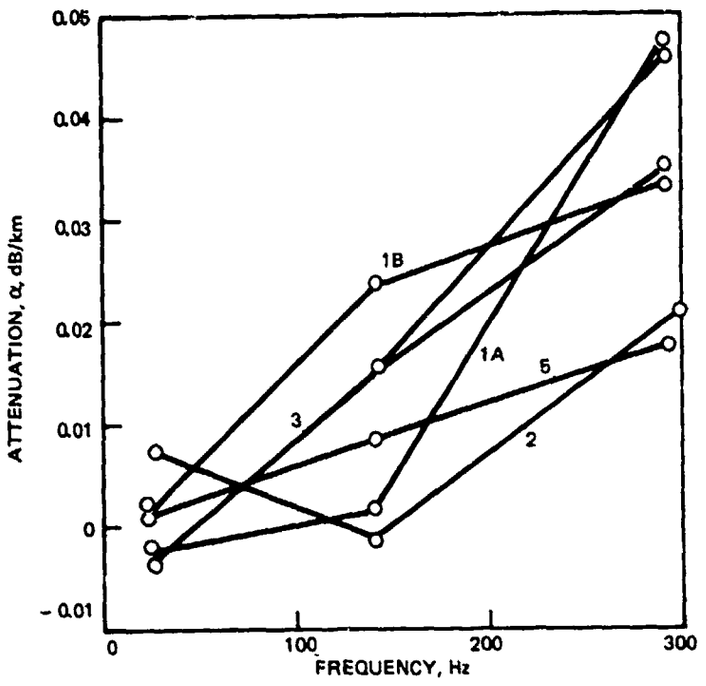

(CONFIDENTIAL)

(U) Figure 6. Attenuation (slope of least squares fit) for observed data.

COMPARISON OF COMPUTED AND OBSERVED DATA (U)

(U) Normal mode runs with random phase addition are labeled "NMRP" in Table 3. Comparison of the four normal mode runs for data averaged in bins with the random phase runs just below them indicate that the results are essentially equivalent. We therefore are confident in using these and other random phase computations to represent the normal mode results.

(U) From Table 3, H_0 and α can be compared for normal mode and observed data for Sites 1, 3, and 5 at each of the three frequency ranges. Figure 7 shows H_0 for these cases. The outer limits of the equivalent value from the observed data from Fig 5 are shown as a cross-hatched area. The values for H_0 for normal mode are larger than those for the observed data at the low frequency but fit within the large spread for the data at the two higher frequencies. This suggests that the source strength used in reducing the observed data at the low frequency may have been too low. The true source strength was probably 1.5 dB higher, with true losses greater by that amount. Let us look at the differences between individual sites to be more specific.

(C) Figure 8 shows the differences between H_0 as derived from the data and the normal mode losses. The two Site 1 runs, 1AP7 and 1BP1 were over nearly identical paths and should yield the same results. Reference 1, page 74, concludes that tow 1AP7 is in error at 140 Hz by +2 dB. Figure 8 supports this conclusion. Part of the problem at Sites 1A and 1B results because the ranges were only to 200 and 298 km for these two tows, respectively, or three and five range bins. The parameters resulting from these least squares

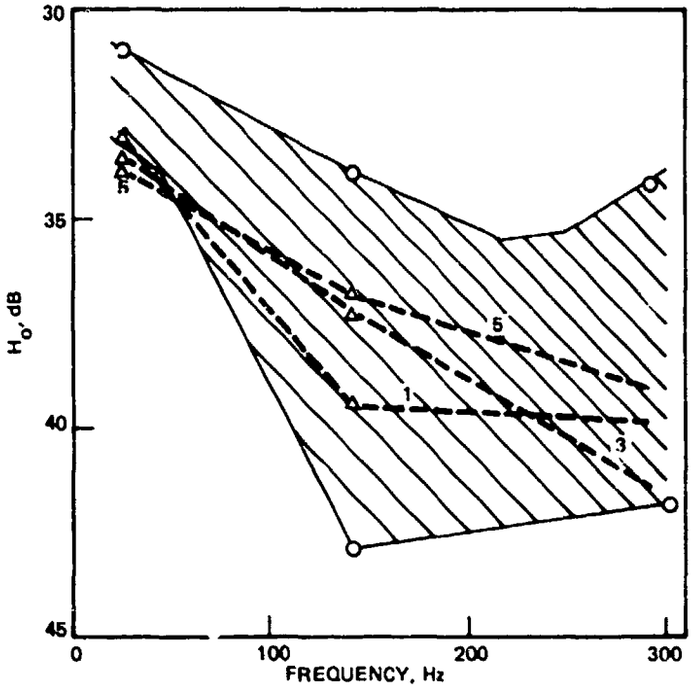

(CONFIDENTIAL)

(U) Figure 7. Zero intercept of least squares fits to loss – 10 log (r) for computed losses. The observed data from Fig 5 lies within the cross-hatched area.

fits are therefore more variable than those for the usual 15 range bins. However, the two values for Site 3 also diverge markedly on the scale of this figure.

(C) Site 5 is a special problem. While the hydrophones at Sites 1 and 3 were on the bottom of the flat alluvial fans, that for Site 5 was on a hill 700m above and 6 km distant from the fan. This hill, with over a 6-deg slope, will intersect all uptravelling rays from an 18-m source that would otherwise reach the receiver. These rays will, in general, reflect to a point beyond the receiver. The deeper source depth of 77m used at 22 Hz will allow rays up to 3.6 deg from the horizontal at the source to clear the slope and reach the receiver. Thus, to compare with Sites 1 and 3 data and also with the normal mode results, Site 5 loss data should be decreased by nearly 3 dB at the two higher frequencies and a lesser amount at 22 Hz. Such a decrease would result in a corresponding decrease in H_O. Thus, the small differences in H_O for Site 5 shown in Fig 8 are incorrect and should be larger by perhaps 1 to 2.5 dB. With this uncertain result, we nevertheless average the four differences at the low frequency in Fig 8 and get an estimate of source strength error of between 1.5 and 2 dB.

(U) At the two higher frequencies, an ever larger underestimation of the source strength is suggested. However, the larger scatter of the differences makes this less certain. Also, the larger attenuation rates here leave open the possibility of other explanations. In the low-frequency case, source level appears to be the only available explanation.

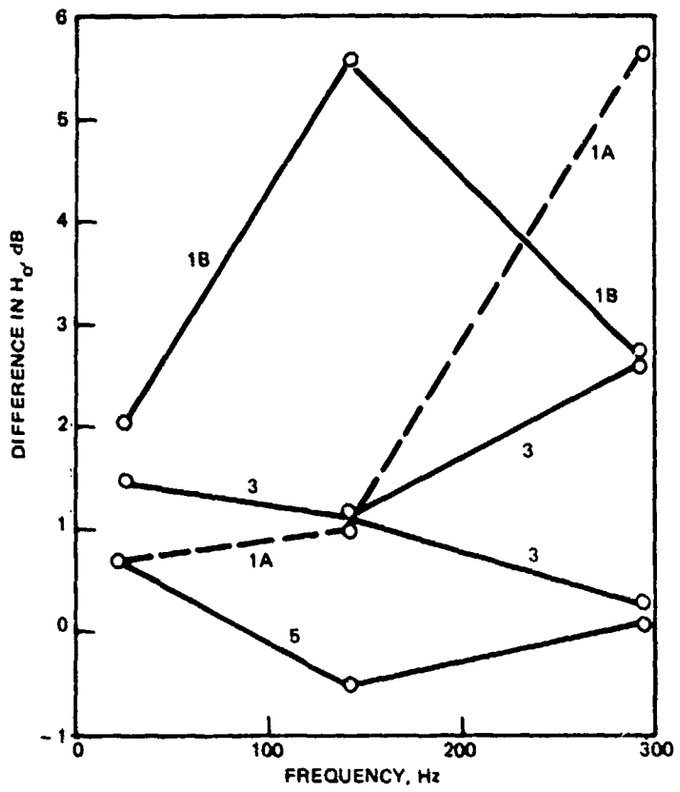

(UNCLASSIFIED)

(U) Figure 8. Zero intercept for observed data minus zero intercept for computed data.

(U) Figure 9 shows the attenuation, α, for the normal mode data. Again, the area occupied by the observed data from Fig 6 is cross-hatched. The computed attenuation is definitely greater than the observed attenuation. Because α is a measure of bottom loss, we must turn to the geo-acoustic bottom models to clarify the differences. In the following sections, we will compare our approximate models of the sediments with the ARL models, which were derived from Bearing Stake data. We will show examples which indicate the sensitivity of the reflection loss to some of the sediment parameters. Finally, we will show some of the fundamental differences between the normal mode and ray theory reflection losses. However, in general, we will be unable to explain the differences in α in Fig 9.

BOTTOM REFLECTION (U)

(U) Figures 10 to 12 show the sediment acoustic models for Sites 1, 3, and 5. Three quantities, sound speed, sound absorption, and density, are shown as a function of depth for each site. The approximations to these models used in the normal mode computations are also shown (broken lines). In the normal mode model, the squared index of refraction is a linear function. The sound speed is therefore not linear but slightly curved, as seen in the figures. The index of refraction is a complex number and the imaginary part is proportional to the absorption, a, given by

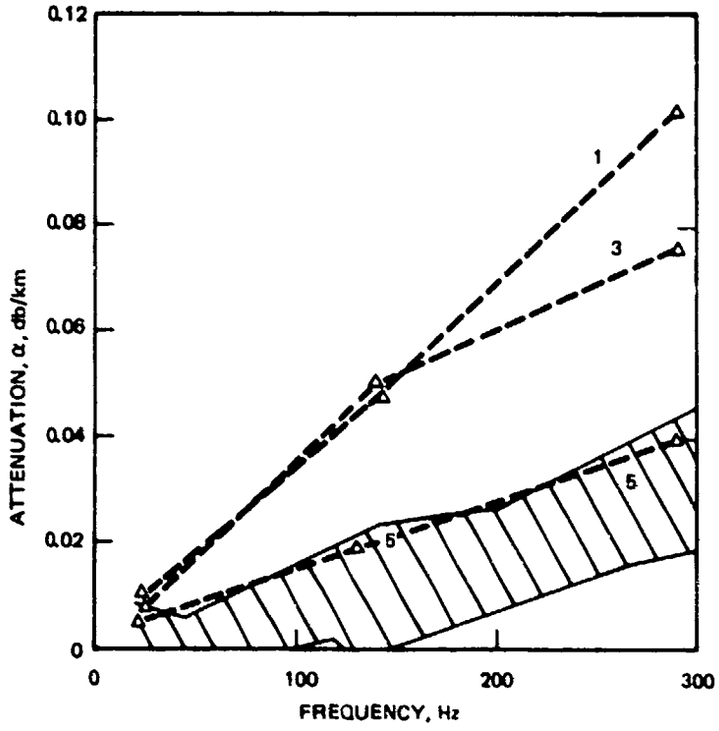

(CONFIDENTIAL)

(U) Figure 9. Attenuation for computed losses. The observed data from Fig 6 lies within the cross-hatched area.

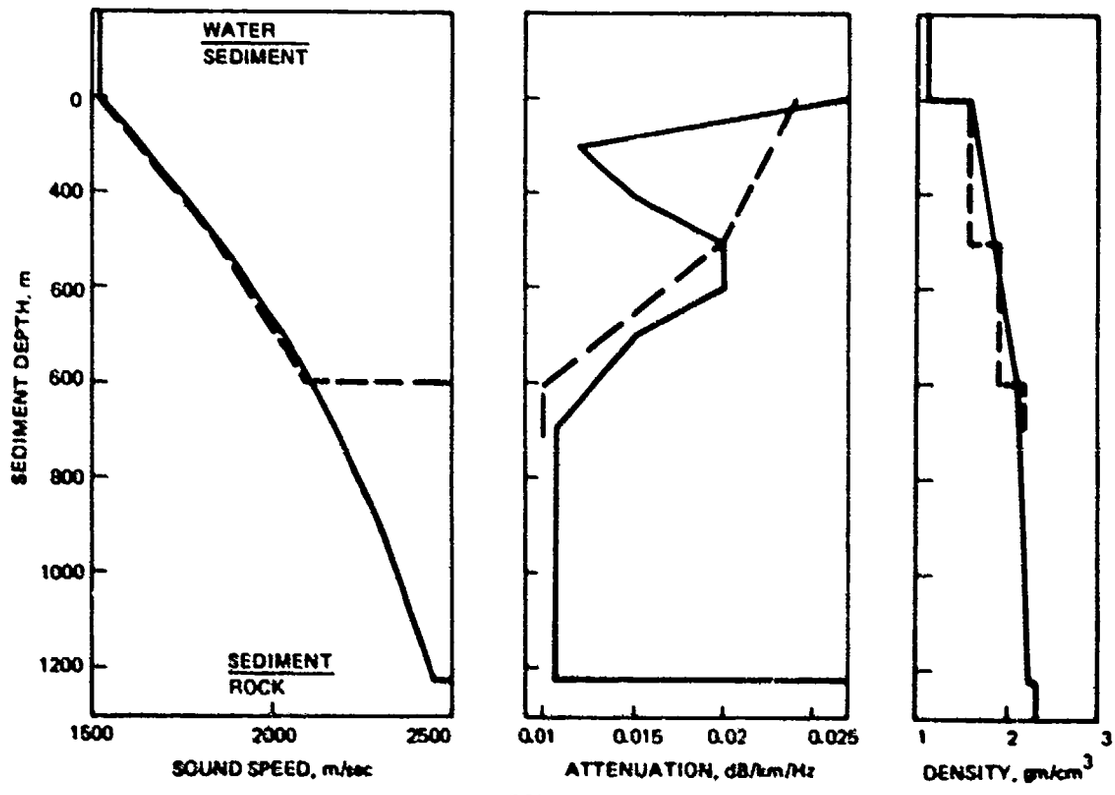

(CONFIDENTIAL)

(U) Figure 10. Sediment model for Site 1 and two layers fitted to it for normal mode computations.

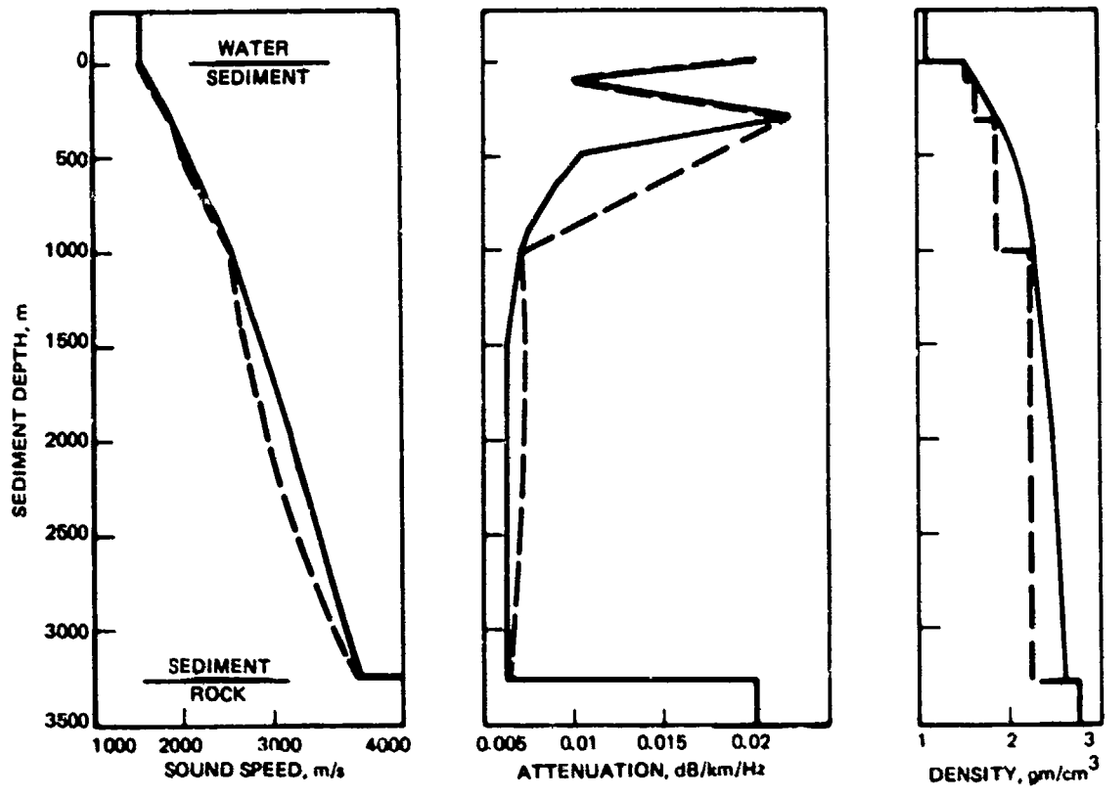

(UNCLASSIFIED)

(U) Figure 11. Sediment model for Site 3 and four layers fitted to it for normal mode computation.

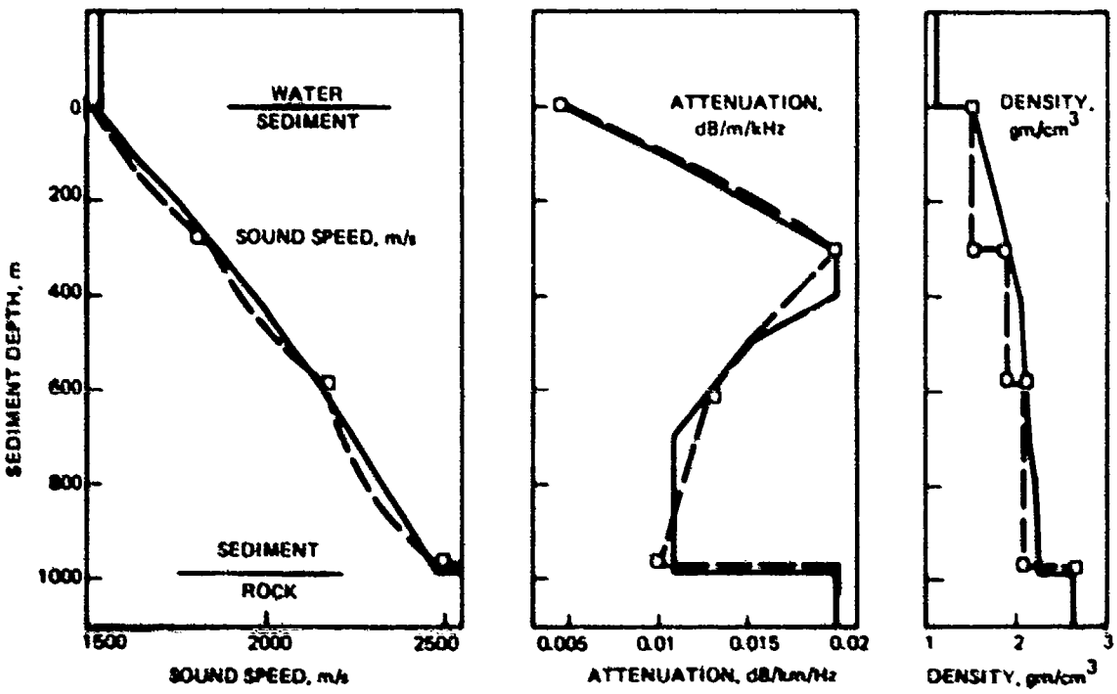

(UNCLASSIFIED)

(U) Figure 12. Sediment model for Site 5 and three layers fitted to it for normal mode computation.

$$a = -20 \log(e)\, \omega\, \mathrm{Im}\, n/C_o \qquad (8)$$

where ω is the angular frequency, n is the index of refraction, and a is in dB/m. In the normal mode model, the density is a step function, constant in each layer.

(U) The fit to Site 1 was made at an earlier date than the other two, and less care was used in fitting α near the top of the sediment. Also, it was only carried to a depth of 600 m. Rays with grazing angles greater than 43 deg will penetrate to this depth. The equivalent mode has an attenuation of 0.1 dB/km at 25 Hz. Thus, in the first 100 km, the field may be unduly strengthened by reflections from this too-shallow basement. However, the poor fit to a in the first 300 m of sediment depth is a greater cause of error. Figure 13 shows the reflection coefficients obtained from this model, the observed reflection coefficients, and the ARL reflection coefficients. It can be seen that the reflection losses for the normal mode model are consistently greater than those for the ARL model for the first 25 deg of grazing angle.

(U) In Fig 13 and those following, the observed reflection losses are plotted at the center of 5-deg grazing angle bins. The standard deviation of these points is great enough to include the ARL loss curve in each case. Therefore, the ARL curves, which are based on computed reflection coefficients and ray paths through the sediment, are believed to be a more reliable estimation of reflection loss than the observed loss points. The ARL sediment models of Fig 10 to 12 were derived by modifying the sediment attenuation until the computed loss curves matched the observed curves sufficiently well at the higher frequencies. The assumption that attenuation in the sediment is proportional to frequency was made to compute reflection losses at the lowest frequencies.

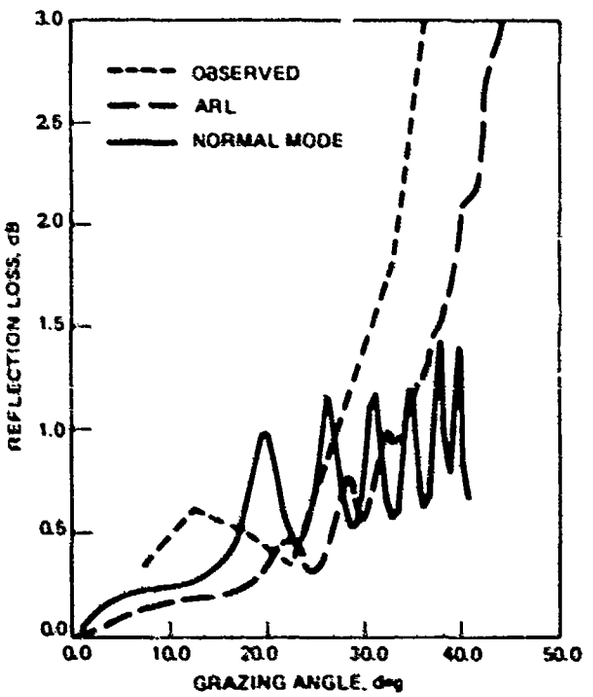

(CONFIDENTIAL)

(U) Figure 13. Reflection losses for Site 1 at 25 Hz.

(U) The normal mode reflection losses are a ratio of the up- and down-going energy at the water-sediment interface for each individual mode. Each mode corresponds to a specific grazing angle determined by its phase velocity. Four reasons for the discrepancy between the normal mode and ARL losses are apparent. First, the differences in the model, as was discussed for Site 1, cause some discrepancies. These differences arise because the normal mode is limited in the number of layers that can be used in the sediment. The number of sediment plus water layers is limited to 12. Secondly, the ARL results are for 1/3-octave frequency bands, while the normal mode losses are for a discrete frequency. Thus, the strong interference patterns seen in the normal mode losses would be largely averaged out if a band of frequencies were used. The average loss would be near the bottom of the interference beats.

(U) Thirdly, as discussed, the paths refracted in the sediments are different for the two models. The ARL paths are for a fixed total loop length, while the normal mode paths are for a fixed phase velocity. This difference becomes noticeable above 20 deg and may account for much of the large discrepancy at very high grazing angles.

(U) Lastly, the total upgoing energy of the normal mode reflection loss includes that arriving from multiple reflections from the underside of the sediment. Thus, the only significant energy loss in the normal mode model is that to sediment attenuation.

(U) In Fig 13 to 15, the reflection losses for Site 1 are compared in three frequency ranges. At the two lower frequencies, the normal mode losses are greater to about 25 to 30 deg grazing angle, where they cross the ARL losses and become less. It appears that if the 290-Hz normal mode computations were carried out to this range, they would behave in the same way.

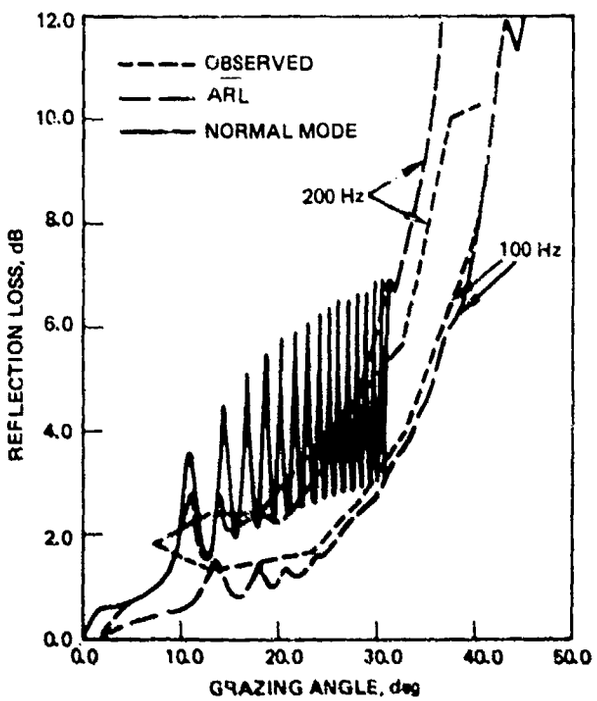

(CONFIDENTIAL)

(U) Figure 14. Reflection losses for Site 1. Normal mode losses at 140 Hz compared with observed and ARL losses at 100 and 200 Hz.

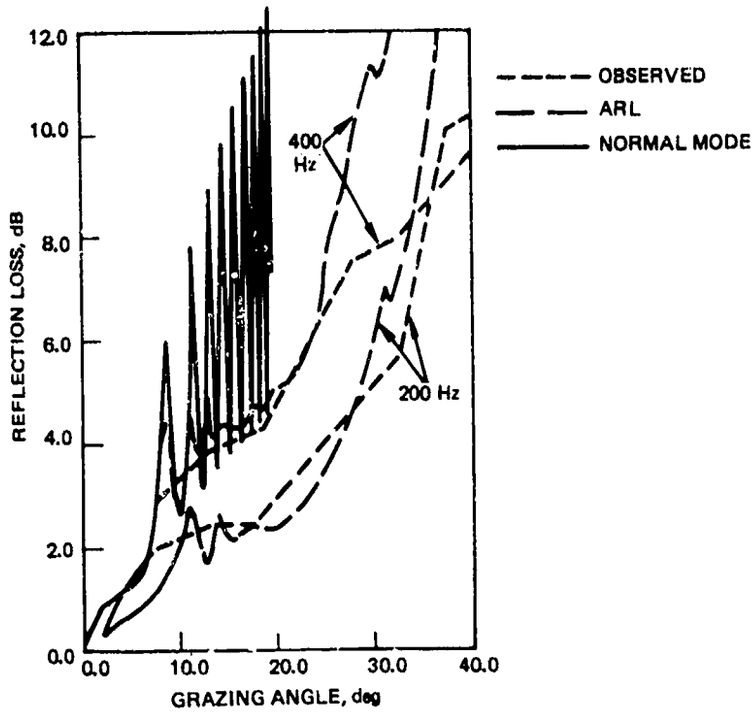

(CONFIDENTIAL)

(U) Figure 15. Reflection losses for Site 1. Normal mode losses at 290 Hz compared with ARL and observed losses at 200 and 400 Hz.

(U) In Fig 16 to 18 for Site 3, the reflection losses are greater for the normal mode only to 5 to 8 deg grazing angle and then are decidedly less than the ARL losses. For Site 5 (Fig 19 to 21), the two losses agree well to beyond 20 deg, where the normal mode losses are again smaller. An exception is the 100- and 200-Hz ARL curves, which have high losses at grazing angles of 1 to 3 deg, as do the observed loss curves The normal mode losses do not show this large loss, although the 140-Hz case is somewhat steeper near zero grazing angle than the other two. A further investigation shows similar effects in the normal mode losses.

(U) Figure 22 shows the reflection loss at Site 5 for the first 5 deg of grazing angle for six different frequencies as evaluated at the normal modes. The curves in the figure start from the first mode with phase velocity greater than the bottom-water sound speed. The reflection coefficient should be approximately zero at zero grazing angle, so the curves can be arbitrarily continued to this point. Only the 90-Hz curve would leave a serious question of how to connect it to zero. It is apparent, though, that a pronounced interference-like peak occurs near 90 Hz.

(U) The Rayleigh reflection coefficient is 0.51 at 1 deg grazing angle (as a ratio of intensities) and is independent of frequency. This equal partition of energy permits destructive phase interference between the two parts. A second possible mechanism for the loss peaks is that the phase of the incident sound at the sediment surface and the refracted path in the sediment can combine to keep as much energy as possible reflecting repeatedly from the underside of the sediment. This would then maximize loss by absorption in the sediment.

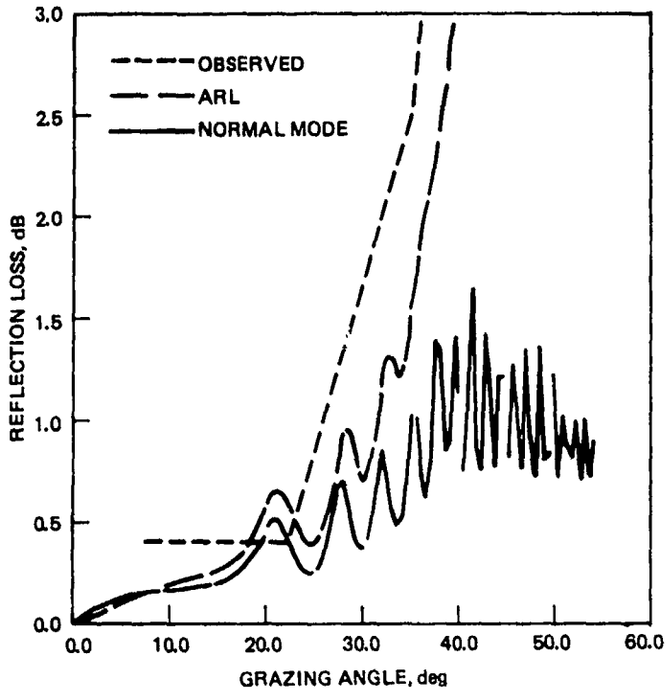

(CONFIDENTIAL)

(U) Figure 16. Reflection losses for Site 3 at 25 Hz.

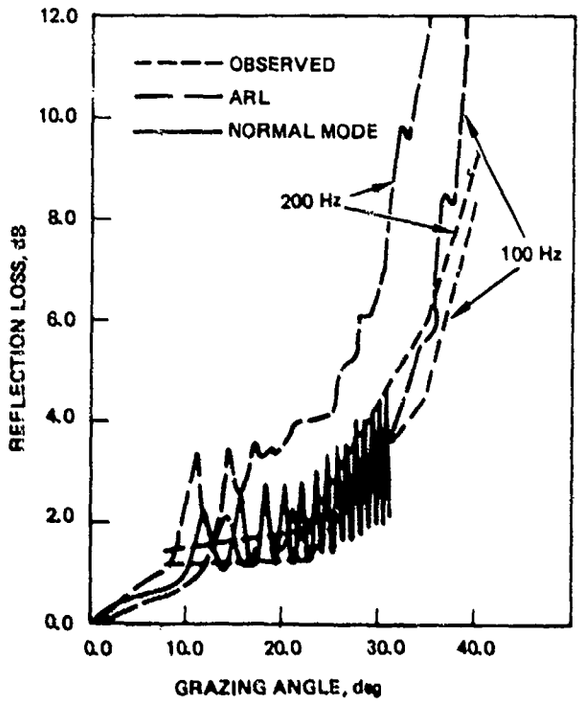

(CONFIDENTIAL)

(U) Figure 17. Reflection losses for Site 3. Normal mode losses at 140 Hz compared with observed and ARL losses at 100 and 200 Hz.

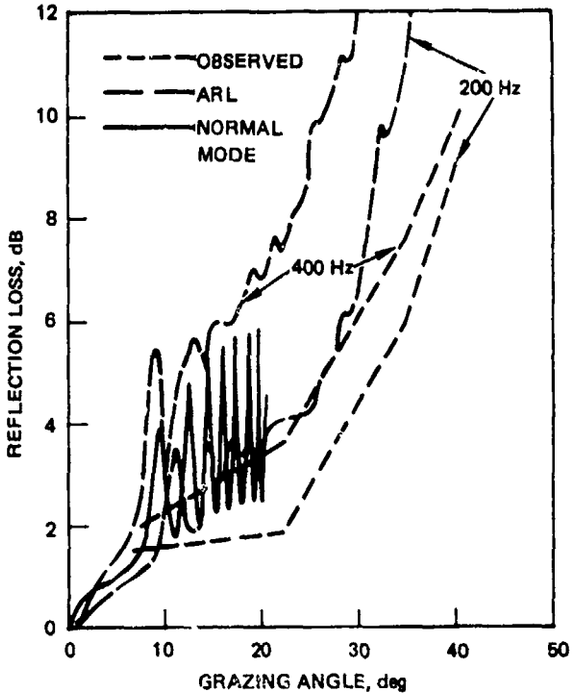

(CONFIDENTIAL)

(U) Figure 18. Reflection losses for Site 3. Normal mode losses at 290 Hz compared with observed and ARL losses at 200 and 400 Hz.

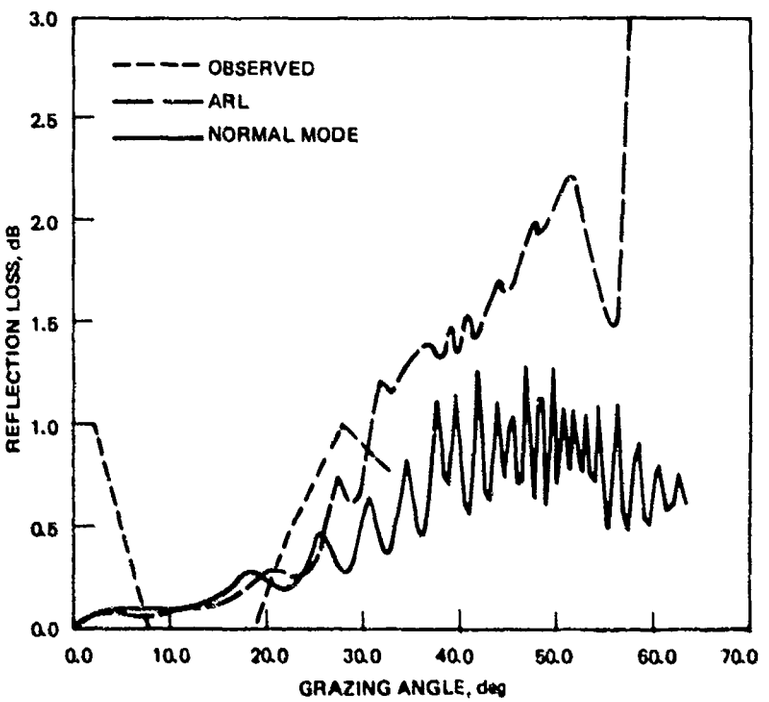

(CONFIDENTIAL)

(U) Figure 19. Reflection losses for Site 5 at 25 Hz.

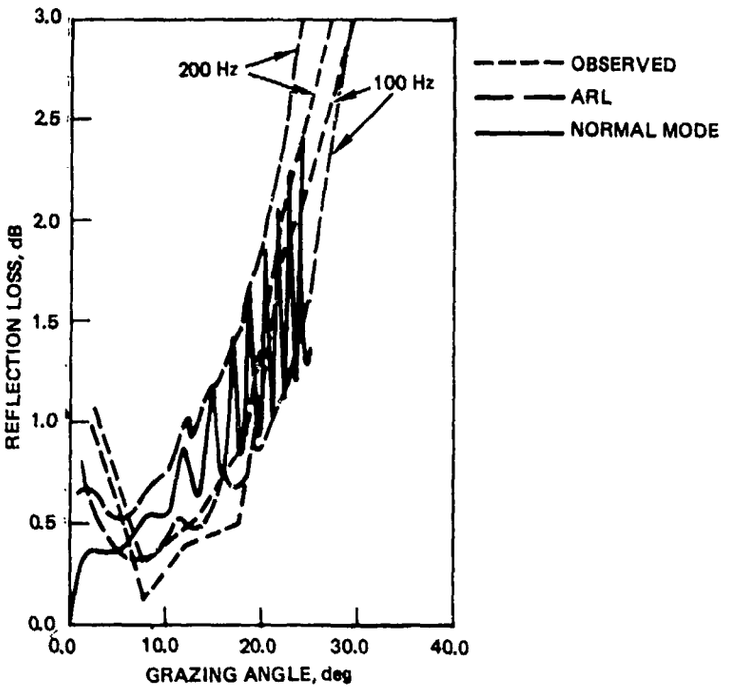

(CONFIDENTIAL)

(U) Figure 20. Reflection losses for Site 5. Normal mode losses at 140 Hz compared with observed and ARL losses at 100 and 200 Hz.

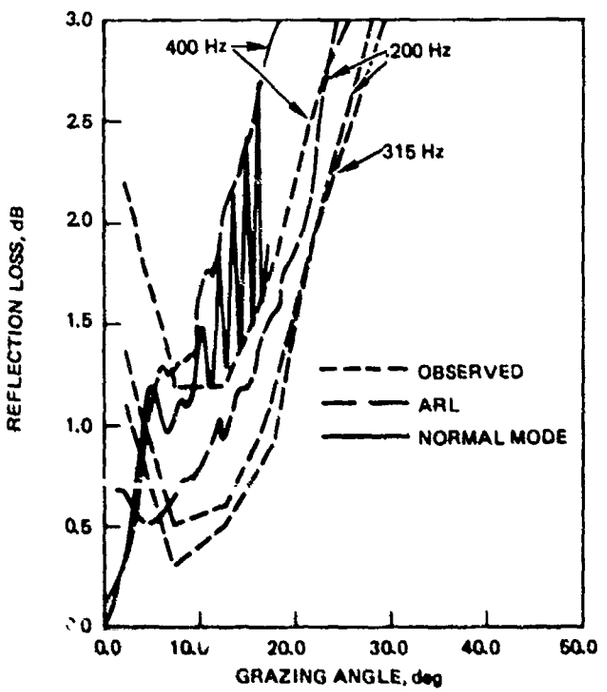

(CONFIDENTIAL)

(U) Figure 21. Reflection losses at Site 5. Normal mode losses at 290 Hz are compared with observed losses at 200, 315, and 400 Hz and ARL losses at 200 and 400 Hz.

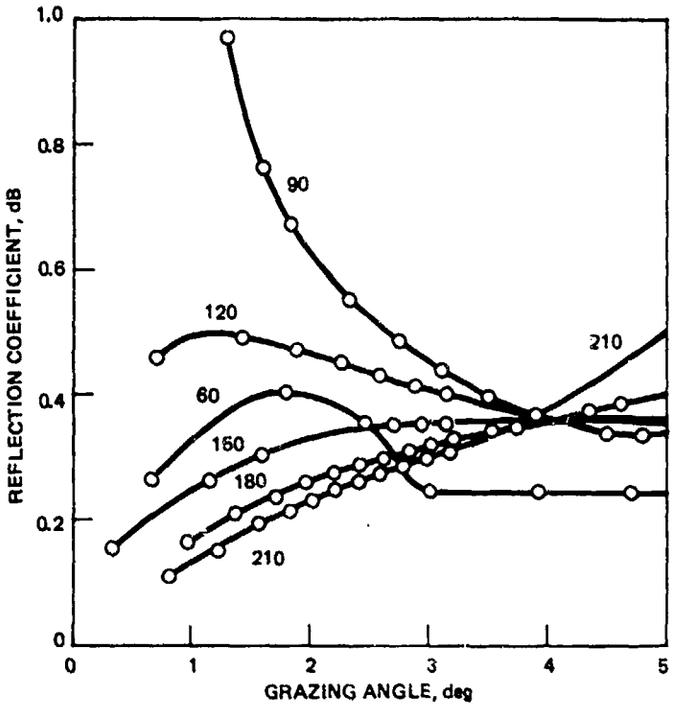

(UNCLASSIFIED)

(U) Figure 22. Reflection loss for Site 5 at six frequencies from 90 to 210 Hz.

(U) No attempt has been made to verify the loss mechanism suggested above. We have shown that normal mode sometimes predicts high bottom losses in the first 5 deg of grazing angle. The ARL reflection coefficients show high losses at 100 and 200 Hz, and the Site 5 data show relatively high losses for low grazing angles at all frequencies. Slow sound speed at the sediment surface is a first requirement for predicting this effect.

(U) A higher bottom loss effect, similar to the above but less pronounced, is apparent in the data for Site 4 in Ref 5 for just one of the five frequencies, 50 Hz. At Sites 1 and 3, low grazing angle data were generally not available, or possible, because the sound speed at the source was substantially higher than at the bottom. Because the sediment sound speed at these two sites is equal to or greater than the water sound speed, a well-behaved reflection coefficient at low angles is expected.

(U) In conclusion, a comparison of Fig 6 and 9 shows that the attenuation α for the modeled propagation is two to four times greater than for the observed propagation. Because bottom loss is the principal mechanism producing attenuation, we examine bottom loss values. At Site 1, the bottom losses at low grazing angles, as determined by the normal mode program, are greater than the observed losses as modeled by ARL by up to 40 percent. However, at Sites 3 and 5, the losses are reasonably similar. The higher losses at Site 1 can be explained by an imprecise modeling of the sediment attenuation. It appears then that the ARL sediment models produce the desired reflection losses. These reflection losses do not produce the observed attenuation. The measured reflection loss data then are larger than the actual losses in the long-range propagation.

(U) Several checks should then be considered. First, other wave theory programs should be used to model the propagation, using the ARL sediment models to confirm that the resulting attenuation is too large. Second, because the observed attenuation is very low compared with other oceans, small corrections might be sufficient. The discrepancy here is not large in magnitude. Selecting lower reflection losses still within a standard deviation of the mean might be enough to obtain agreement. Third, with the size of the correction in mind, the experimental procedure should be reviewed to find possible sources of error.

SEASONAL VARIATION (U)

(C) Colborn (Ref 8) has reported on seasonal variation in sound speed in the Indian Ocean. Seasonal variation in sound propagation is small or moderate at the bottom-limited sites in the Indian Ocean. This is because propagation by the bottom-reflected paths depends much more on bottom characteristics than on sound speed profiles. In this section we will note the difference in propagation loss between the extreme sound speed profiles of the year for each site. One can, with reasonable assurance, assume the propagation loss for other profiles will lie between these extremes.

(U) The main effect that the sound speed profile exerts on this bottom-reflected propagation is to determine the bottom grazing angle. A second effect is to change the loop length or range between bottom encounters, but the deep part of the profile, which does not change perceptibly with season, accounts for the major part of the loop length. Therefore, it is the first effect, the grazing angle, which is most important in seasonal variation. The sound speed at the source determines the minimum grazing angle of rays at the bottom.

(U) Characterizing the propagation by season, therefore, requires choosing a source depth. We have chosen 100 m as a depth of general tactical interest. We will therefore classify profiles according to their sound speeds at 100 m depth. Specifically, we will select profiles with maximum and minimum sound speeds at 100 m depth and assume these will give maximum and minimum propagation of sound for a source at that depth.

(C) Seasons in the Northwestern Indian Ocean consist of two monsoon seasons and the two transition seasons between them (Ref 8). The summer monsoon extends from June through September. October through November is an intermediate season. The winter monsoon extends from December through February, and March through May is a transition season.

SEASONAL PROFILES (U)

(C) Archived sound speed profiles from the vicinity of Sites 1, 3, 4, and 5 were divided into these four seasons. Site 4 was included, although computations for it are not included in this report. Profiles with maximum and minimum sound speed at 100 m were selected for each site and season. The maximum and minimum profiles for the entire year were then selected. These are listed in Table 4. It turned out that the maximums for the four sites occurred in the winter and in the summer monsoon (one each) and in the spring intermediate season (two). The minimum profiles occurred in the spring intermediate

8. NUC Technical Paper 502, "Sound-Speed Distribution in the Western Indian Ocean," J.G. Colborn, Feb 1976.

Site	Season	Lat	Long	Sound Speed at 100 m, m/s	Minimum Grazing Angle, deg
MAXIMUM					
1	WM	22° 31′	61° 30′	1533.3	8.8
3	SM	15° 30′	63° 43′	1541.3	10.3
4	SI	5° 2′	52° 12′	1543.0	0.9
5	SI	8° 16′	63° 46′	1541.6	5.7
MINIMUM					
1	SM	23° 10′	60° 20′	1520.2	4.6
3	FI	20° 0′	63° 0′	1520.2	4.0
4	SM	6° 47′	50° 8′	1508.0	0.0
5	SI	9° 13′	60° 13′	1524.6	0.0

(CONFIDENTIAL)

(U) Table 4. Profiles with maximum and minimum sound speed at 100 m depth. Seasons in which profiles were observed are classified as winter and summer monsoon (WM, SM) and spring and fall intermediate (SI, FI) seasons.

season (one), in the summer monsoon (two), and in the fall intermediate season (one). For Site 5, both the maximum and minimum profiles were observed during the spring intermediate season. One can therefore make no obvious correlation between time of the year and sound propagation in this part of the Indian Ocean.

(U) Table 5 gives the interfaces of the extreme sound speed profiles as selected for normal mode computations. Sound speeds are given at 100 m. Some of these are the points at which the near-linear layers crossed 100 m depth and differ slightly from the equivalent observed profile sound speeds of Table 4. It can be seen that sound speed profiles with minimum sound speed at 100 m do not necessarily have minimum sound speeds at other depths. In many cases, the sound speed of a minimum profile exceeds that of the maximum profile at some depth. Thus, computed propagation loss will only represent extreme cases for 100-m source depths. Also, the Site 5 minimum profile is not bottom limited at 100 m depth, so it represents a special case.

Depth, m	Sound Speed, m/s 1 Max.	1 Min.	3 Max.	3 Min.	5 Max.	5 Min.
0	1532.0	1535.7	1539.3	1541.5	1544.4	1539.7
50		1522.5				1537.2
90				1521.0		
100	1533.3	(1520.6)	1541.3	(1520.6)	1541.6	(1524.4)
150						1512.0
200	1526.0		1517.2		1512.0	
300	1522.7					
400			1508.1	1508.3	1501.7	1501.0
500	1512.4	1506.0				
600						1502.7
800		1501.5				
950				1503.4		
1000	1504.2					
1200					1497.1	
1300			1497.7	1498.1		
1600					1493.0	
1750	1497.2	1496.5	1494.8	1495.0		1494.5
2000					1494.2	
2200	1497.7	1497.7				
2500	1500.9	1500.9	1500.5	1500.5	1500.2	1500.2
3349	1515.3	1515.3				
3555			1516.5	1516.5		
4534					1533.9	1533.9

(UNCLASSIFIED)

(U) Table 5. Sound speed profiles used to compute extremes in seasonal variation. These are fits to profiles which had maximum and minimum sound speed at 100 m depth. Values in parentheses are not layer interfaces but are included for comparison.

VARIABILITY AT 25 Hz (U)

(C) Figures 23, 24, and 25 compare the propagation loss (random phase mode sums) for the maximum and minimum profiles at 25 Hz. The source depths for these three computations were 102, 77, and 77 m, as given in Table 1. The parameters resulting from least squares fits to these runs are given in Table 3. The source depths at 77 m are reasonably close to the 100 m at which maximum and minimum sound speeds were selected. The sound speed for the Site 5 minimum profile at 77 m depth is 1530.3 m/s, so there is over 200 m of depth excess, compared with 360 m depth excess at the 100-m depth. Therefore, similar propagation results can be expected.

(U) The seasonal propagation loss variability as indicated by these three comparisons is small. The largest difference, Site 1 at maximum range, is only 2 dB. This is to be expected because the bottom reflection loss dominates the propagation and does not change with season. Site 5 with bottom excess can be more complicated and will be discussed further in the next section.

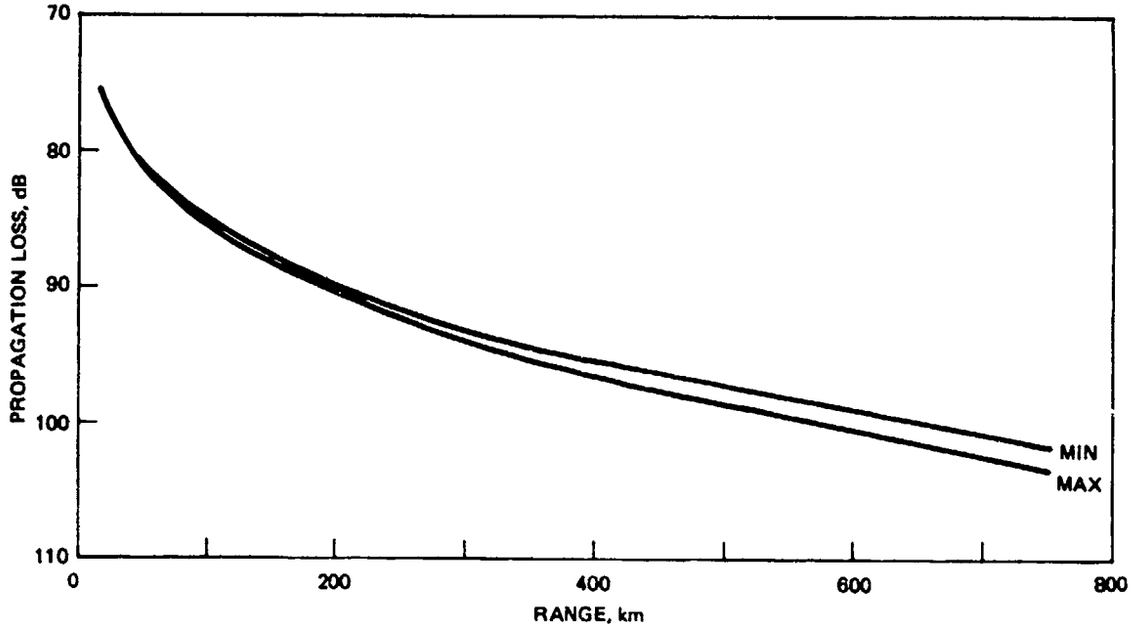

(UNCLASSIFIED)

(U) Figure 23. Propagation losses computed for seasonal extreme profiles for Site 1, 25 Hz using random phase mode addition. Source is at 100 m, receiver is at the bottom.

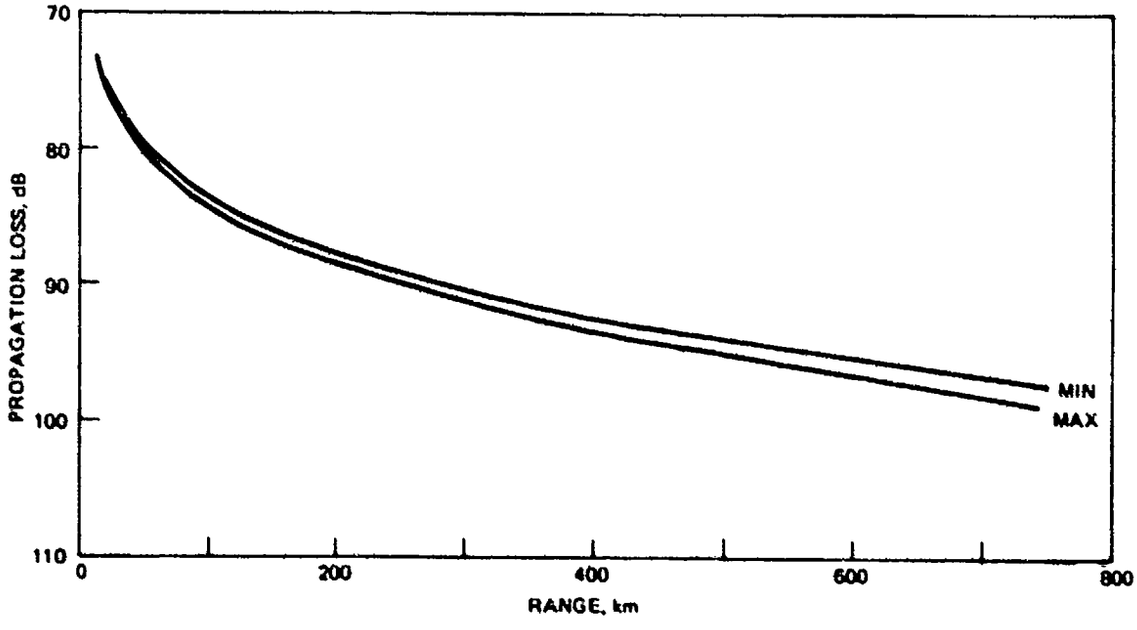

(UNCLASSIFIED)

(U) Figure 24. Propagation losses for seasonal extreme profiles for Site 3, 25 Hz.

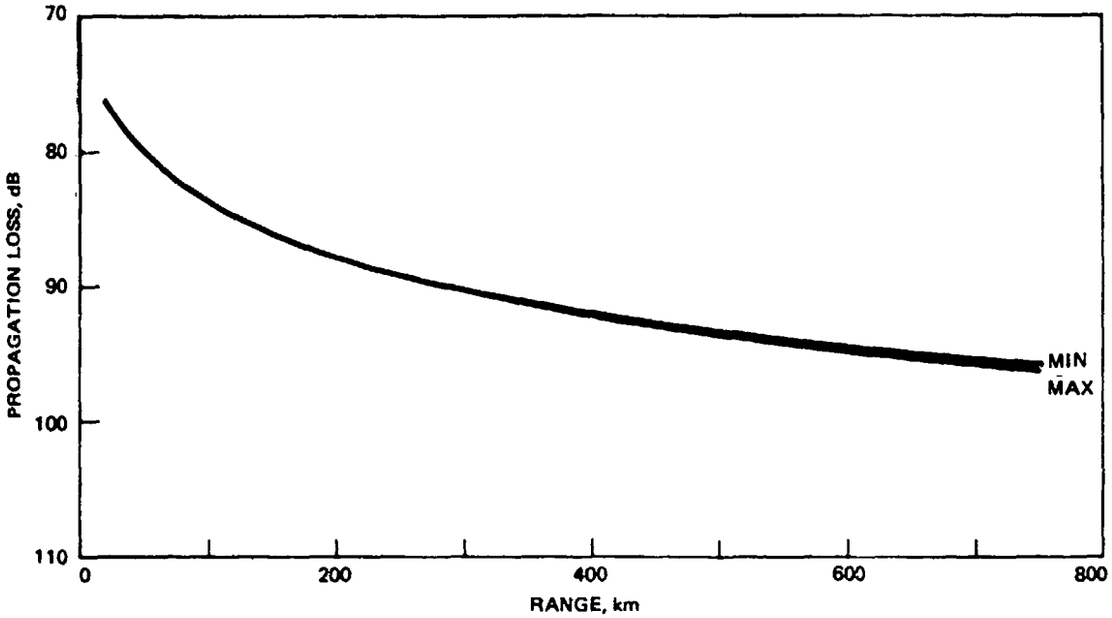

(UNCLASSIFIED)

(U) Figure 25. Propagation losses for seasonal extreme profiles for Site 5, 25 Hz.

(U) In Table 3, the value for α for Site 1, 25 Hz, does not lie between those for the Site 1 minimum and maximum profiles. A reason for this is that the Site 1 profile happens to be almost exactly equal to the minimum profile at 100 m depth. In fact, because of the curve fit, it has a sound speed there of 0.2 m/s less than that of the minimum profile.

VARIABILITY AT 140 Hz (U)

(U) Propagation losses computed for 18 m source depth do not reflect seasonal variations chosen to be extreme at 100 m depth. Parameters for such cases are given in Table 3 for 140 Hz, but for accurate seasonal comparisons, computations were repeated for sources at 100 m depth. These results are shown in Fig 26, 27, and 28. The values of H_o and α from least squares fits to these computations are given in Table 6. The maximum seasonal difference at this frequency is found for Site 1 at the maximum range (750 Hz) to be 19 dB.

(U) This maximum difference is much larger than the 2-dB maximum difference at 25 Hz. A reason for this can be seen by comparing bottom loss curves. For instance, Fig 13 for Site 1 shows a plateau of low loss extending up to about 15 deg grazing angle at 25 Hz. This plateau only extends to about 6 deg at 140 Hz in Fig 14. The minimum grazing angle of 8.8 deg for the maximum profile therefore excludes this entire low-loss plateau. We conclude that the seasonal variation in propagation to long ranges can be quite large at 140 Hz. The effect depends upon the details of the bottom-reflection loss as a function of grazing angle.

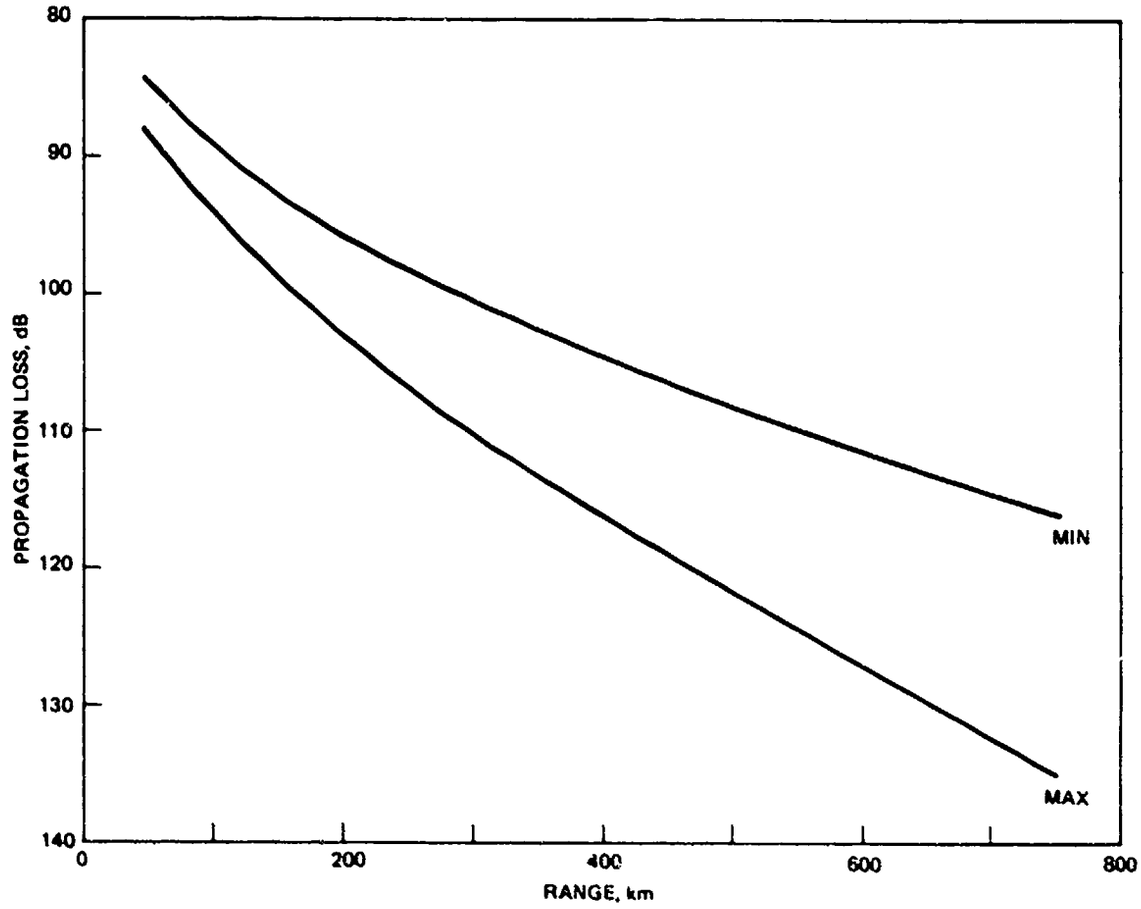

(UNCLASSIFIED)

(U) Figure 26. Propagation losses for seasonal extreme profiles for Site 1 at 140 Hz.

(U) The propagation loss for the Site 5 minimum profile appears to be anomalously high. The attenuation, α, in Table 6 is not really much less than that for the Site 5 maximum profile. This apparent discrepancy is noticeable in Fig 28, where the minimum and maximum curves do not spread as do those in Fig 26 and 27. The reason for this is that the Site 5 minimum profile is not bottom limited at the 100-m source depth. Several different effects are present here, and the propagation cannot be interpreted by reflection coefficients alone.

(U) Propagation for the Site 5 minimum profile would be stronger if source and receiver were at the same sound speed. The bottomed receiver here is at a higher sound speed than the source, and rays up to 6 deg from horizontal at the source do not reach the receiver. A mode theory interpretation is that modes with strongest response at the source depth do not reach the receiver depth (or have a small response there). The first modes that do propagate from source to receiver are not sufficiently large, compared with higher modes, to pull α toward their value. The first of these propagating modes has an attenuation of 0.008 dB/km (0.4 dB loss per bounce with 50-km bounce distance) while the mode sum from Table 6 has an α equal to 0.0173 dB/km.

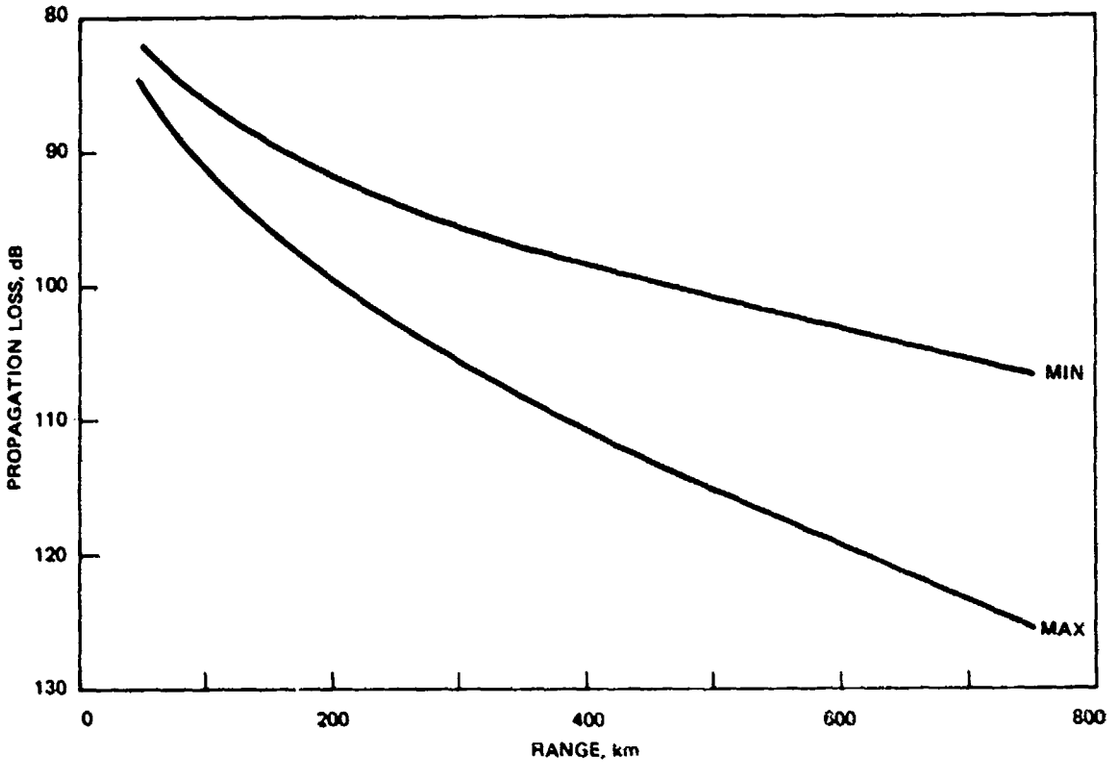

(UNCLASSIFIED)

(U) Figure 27. Propagation losses for seasonal extreme profiles for Site 3 at 140 Hz.

Site	Type	H_o	α	Standard Error of Estimate	n
1MAX	NMRP	40.06 ± 0.30	0.0487 ± 0.0007	0.5605	15
1MIN	NMRP	37.02 ± 0.25	0.0277 ± 0.0006	0.4689	15
3MAX	NMRP	37.70 ± 0.47	0.0402 ± 0.0010	0.8588	15
3MIN	NMRP	35.25 ± 0.21	0.0170 ± 0.0005	0.3860	15
5MAX	NMRP	37.488 ± 0.22	0.0197 ± 0.0005	0.3996	15
5MIN	NMRP	38.32 ± 0.34	0.0176 ± 0.0007	0.6219	15

(UNCLASSIFIED)

(U) Table 6. Fits of $H(r) = 10 \log(r) + H_o + \alpha r$ to the normal mode random phase sums for maximum and minimum profiles for 140 Hz and 100 m source depths.

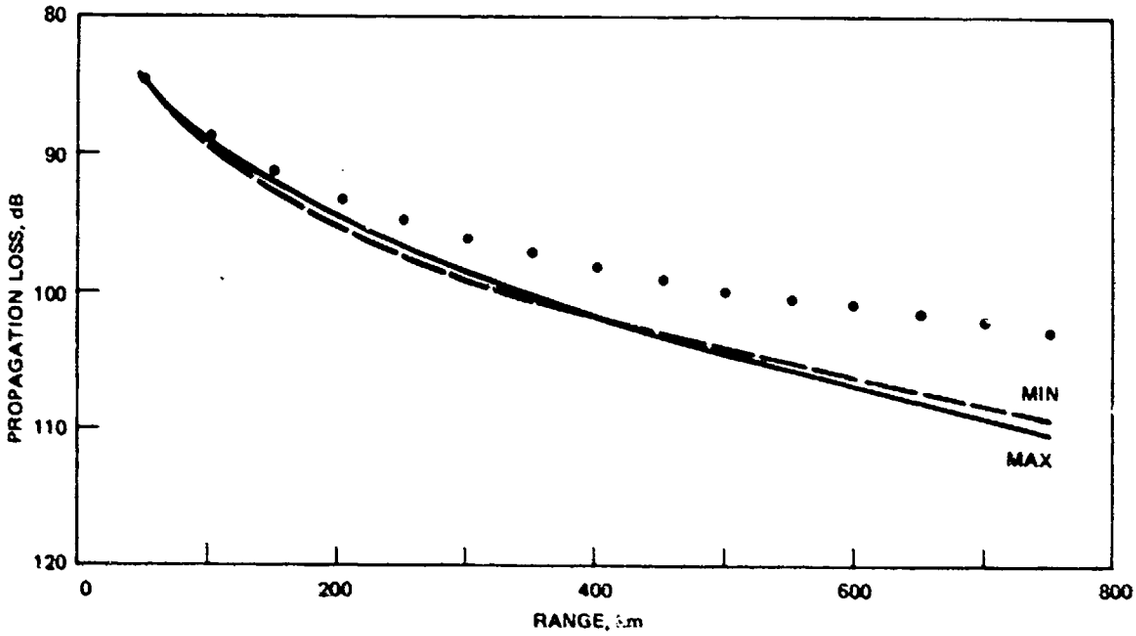

(UNCLASSIFIED)

(U) Figure 28. Propagation losses for seasonal extreme profiles for Site 5 at 140 Hz. The dotted line is for the minimum profile, 3844 m receiver depth, which is near the conjugate depth.

(U) A receiver depth of 3844 m is near the sound speed of the source and the computed propagation loss for this receiver is shown as a dotted curve in Fig 28. Being bottom limited, the maximum profile will have nearly identical losses at the two receiver depths, so at 3844 m depth, a 7-dB seasonal change would be observed.

(U) A second mechanism is less important but adds to the increased attenuation. This mechanism is described in Appendix A and is mentioned here briefly because of its novelty. The sediment at Site 5 has a lower sound speed than does the adjacent water. When sound waves travel near this slow bottom, a dragging effect is felt at the bottom. This can reduce the curvature of the ray path and hold a ray near the bottom for an extended distance. These paths then suffer more than the usual loss of energy into the bottom. Thus, some modes, equivalent to rays vertexing just above the bottom (and the receiver), which would ordinarily add low-loss energy by diffraction to the receiver, are now high-loss and increase α.

(U) The above discussion shows that by choosing a receiver depth 700m above the bottom, a 7-dB seasonal difference in propagation loss at 140 Hz (at 750 km range) is expected at Site 5. However, it also shows that an assessment of seasonal variation is a complicated function of source and receiver depth and frequency, and that generalizations are not always possible.

(U) Seasonal propagation was not computed at 290 Hz because the runs are expensive. It is safe to predict that the seasonal differences at 290 Hz will be at least as great as those at 140 Hz. The source conjugate depth effect seen at Site 5 minimum profile at 140 Hz should be more pronounced at 290 Hz.

PROPAGATION NEAR SEA FLOOR AND SURFACE (U)

(U) Pedersen and Yee (Ref 1) have shown that at Site 1, propagation losses computed by random phase normal modes have a notch of high loss above the ocean bottom. Since this notch occurs at different depths for different source depths, it provides a method for increasing the strength of a target over background noise if the two originate at different depths. For instance, if an array is placed at the depth of a notch for surface ships that create background noise, then a signal-to-noise advantage can be obtained for a submarine target at a different depth. Pedersen and Yee showed that an array 30 m above the ocean floor at Site 1B would have a 3-dB advantage in signal-to-noise ratio over an array on the ocean floor at 25 Hz (both at 200 km range).

(U) In this section we will show that notches also exist at Sites 3 and 5. However, the exact height of the notches above the ocean floor is a function of reflection coefficient, reflection phase shift, depth function beat length, and bottom limiting of some propagation paths. As a result, it will be shown that notch depth varies with season as well as with site. Nevertheless, for a given situation, a near-bottom receiver depth can be found which best suppresses propagation from shallow noise sources at a given depth.

(U) Figures 29 and 30 show computed propagation losses for Site 1 at 25 Hz for source depths of 18 and 100 m. Five standard ranges from 50 to 1000 km have been selected and are used in this and the following figures. The depth scale is divided into two halves: the uppermost 400 m of ocean depth and a lower 400 m, which includes the bottom depth. Curves for this type of propagation are quite flat and uninteresting through the majority of the ocean depth, with only that part near the ocean boundaries being of interest. Random phase mode addition gives a range-averaged result at each depth and makes it possible to see these small effects, which would be very difficult to detect in the highly variable sound field of a single source. The range-averaged result should give a good estimate of the depth variation for noise fields due to many scattered sources at the same depth.

NEAR-BOTTOM SOUND FIELD (U)

(U) At each range in Fig 29, a maximum in propagation loss or notch occurs from 30 to 90 m above the bottom. The distance above the bottom increases steadily with range. In Fig 30 for a 100-m-deep source, the notch varies from 90 to 110 m above the bottom. This notch arises from interference between paths that have reflected from the bottom and those that have not yet touched the bottom. An analysis of this effect will be given in a later section. Here we will discuss the operational implications.

(U) Let the 18-m source depth represent the depth of noise. A shallower depth might be better, but a deep-draft tanker can produce noise near this depth. If the 100-m source represents a submarine, then the best depth for a near-bottom array to detect the submarine is the depth at which the difference in propagation loss most favors the 100-m source depth. This difference between propagation losses of Fig 29 and 30 is shown in Fig 31. The best depth is near the depth of the notch in the loss from the 18-m noise source. Similar curves could be drawn for any two different ranges to noise and signal.

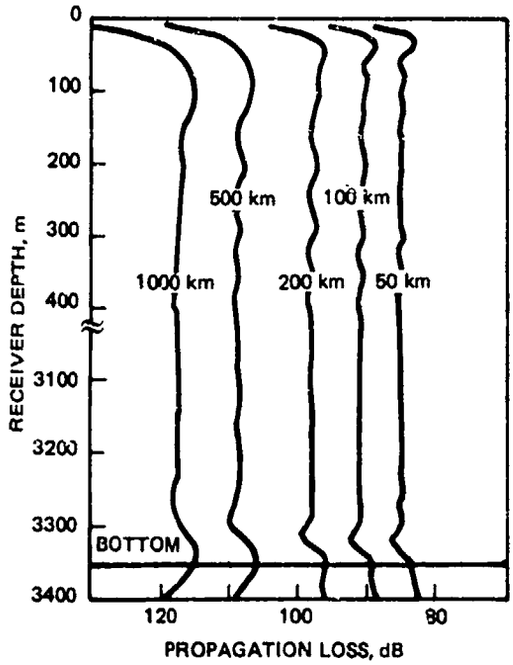

(UNCLASSIFIED)

(U) Figure 29. Propagation loss near the surface and bottom for an 18-m source depth at five ranges, Site 1, 25 Hz. Losses computed by random phase mode addition.

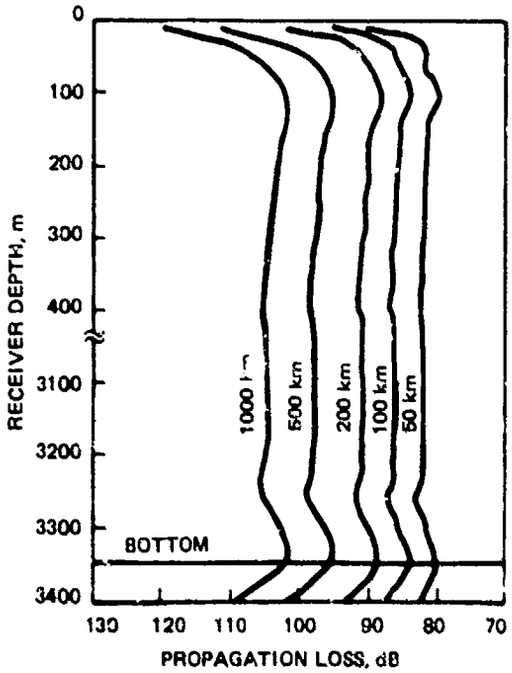

(UNCLASSIFIED)

(U) Figure 30. Propagation loss near the surface and bottom for a 100-m source depth, Site 1, 25 Hz.

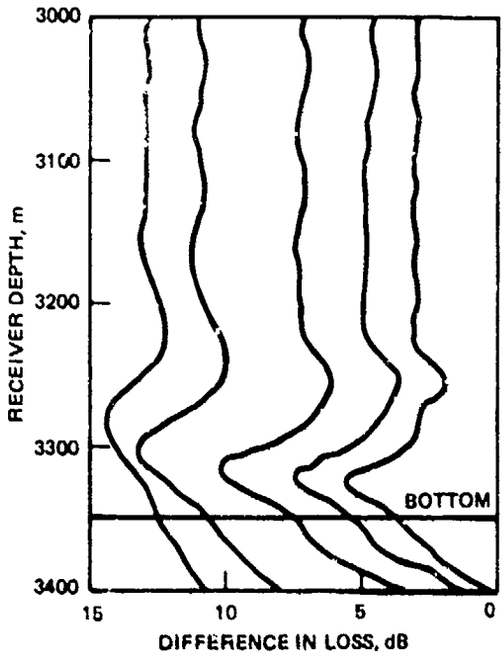

(UNCLASSIFIED)

(U) Figure 31. Differences in propagation loss between the 18- and 100-m source depths of the two previous figures.

(U) A question that can be answered by Fig 31 is how much can be gained by placing an array above the bottom rather than *on* the bottom. The differences between the bottom and the peaks in Fig 31 are 2 to 2.5 dB. Thus, an array suspended about 50 m above the bottom could expect to have a 2-dB advantage in signal-to-noise ratio over one on the bottom at 25 Hz.

(U) Figures 32 and 33 show a similar result for Site 3. At this site, the notch for the 18-m source varies from 25 to 60 m above the bottom. For the 100-m source, the notch is near 90 m above the bottom. The differences between the two losses are shown in Fig 34. Here the difference between a bottomed and suspended array can be from 1.5 to 3 dB.

(U) Figures 35 and 36 show the average propagation losses for Site 5 at 25 Hz. The notch for the 18-m source varies from 25 to 50 m above the bottom. The notch for the 100-m source in Fig 36 is similar to that for the 18-m source, which leads to smaller differences in the difference plot in Fig 37. Here the maximum gain for a suspended hydrophone over a bottomed one is only 1.5 dB, and this only for ranges over 200 km.

(U) The effects of seasonal changes and frequency on the notch effect will be demonstrated by showing six more plots for Site 3. Figures 38 and 39 are for the 18-m source for Site 3 maximum and minimum profile at 25 Hz. The depth of the notches for these two profiles is essentially the same. Only the strength or intensity of the notches varies. Comparing Fig 32 for the standard Site 3 profile with these two shows that it is also very similar, occupying a position between them.

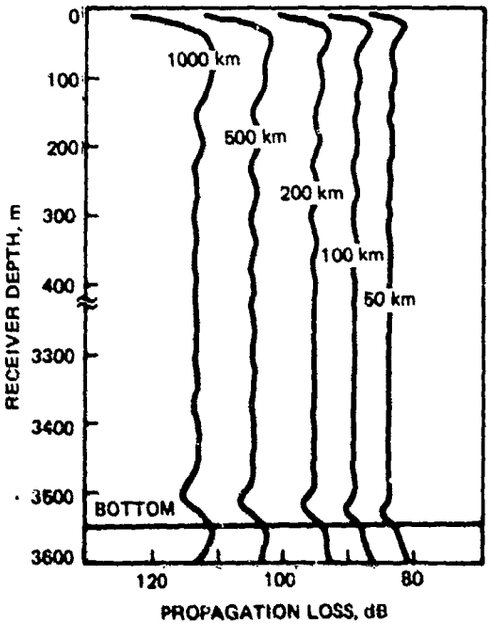

(UNCLASSIFIED)

(U) Figure 32. Propagation loss near the surface and bottom for an 18-m source depth, Site 3, 25 Hz.

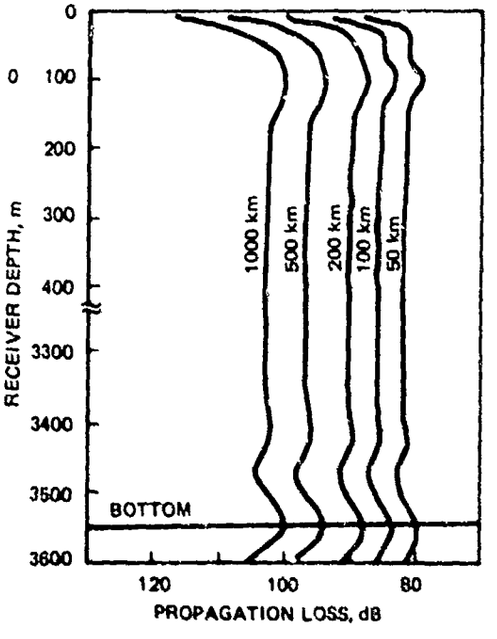

(UNCLASSIFIED)

(U) Figure 33. Propagation loss near the surface and bottom for a 100-m source depth, Site 3, 25 Hz.

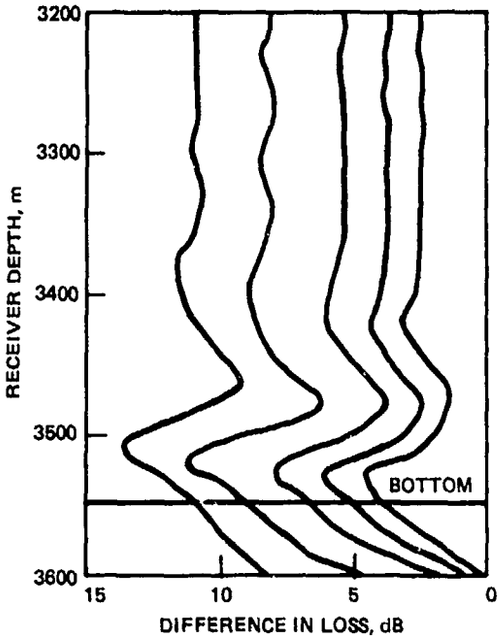

(UNCLASSIFIED)

(U) Figure 34. Differences in propagation loss between the 18- and 100-m source depths of the two previous figures.

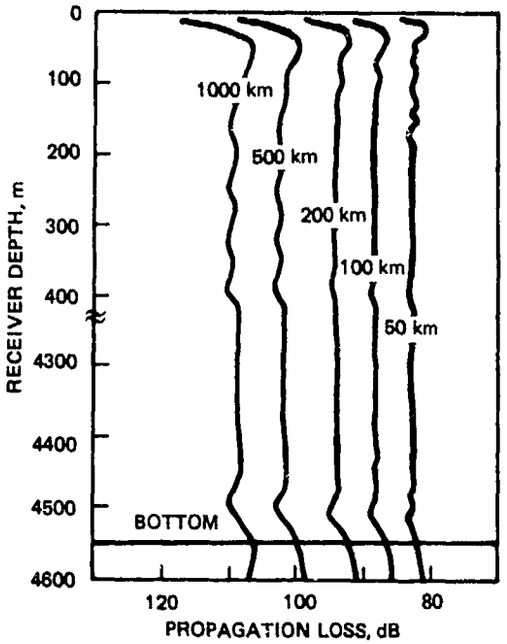

(UNCLASSIFIED)

(U) Figure 35. Propagation loss near the surface and bottom for an 18-m source depth, Site 5, 25 Hz.

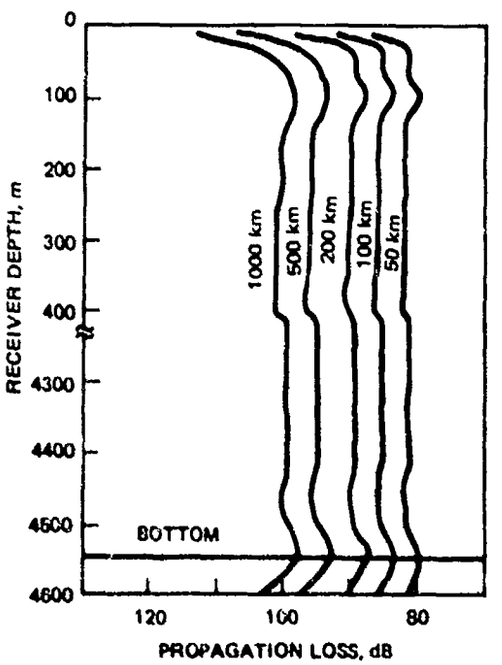

(UNCLASSIFIED)

(U) Figure 36. Propagation loss near the surface and bottom for a 100-m source depth, Site 5, 25 Hz.

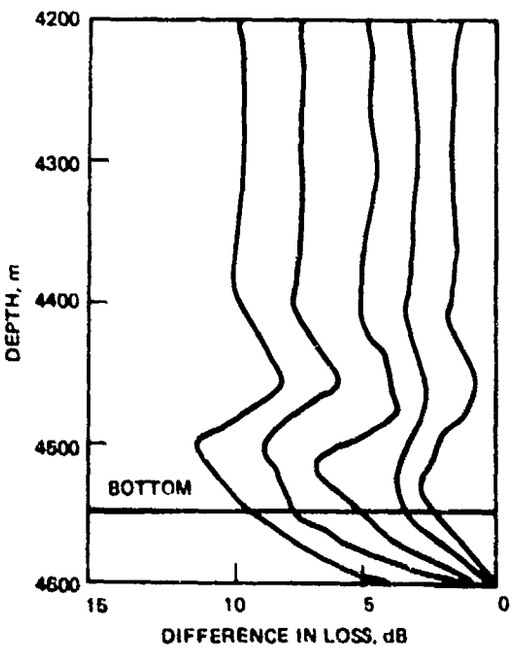

(UNCLASSIFIED)

(U) Figure 37. Difference in propagation loss between the 18- and 100-m source depths of the two previous figures.

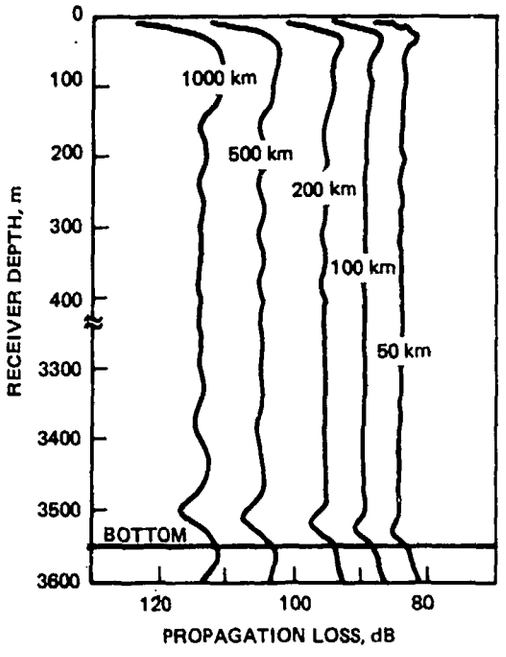

(UNCLASSIFIED)

(U) Figure 38. Propagation loss near the surface and bottom for an 18-m source depth for the Site 3 maximum profile, 25 Hz.

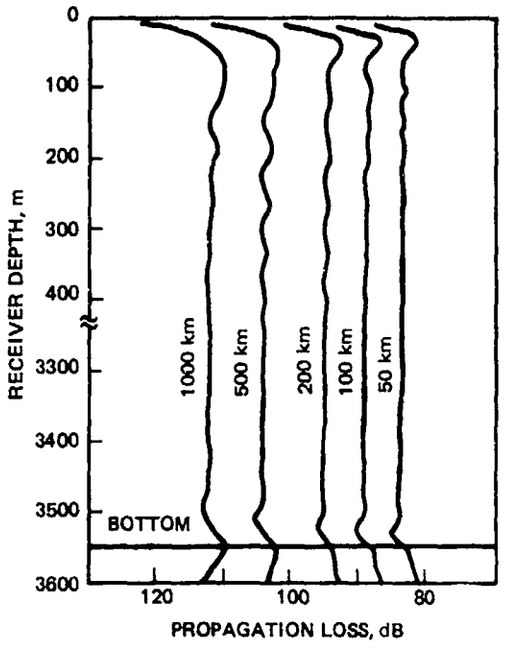

(UNCLASSIFIED)

(U) Figure 39. Propagation loss near the surface and bottom for an 18-m source for the Site 3 minimum profile, 25 Hz.

(U) The plots for the 100-m-deep source are shown in Fig 40 and 41. Here, considerably more seasonal variation is seen. This arises partly because seasonal profiles were selected to maximize sound speed differences at 100 m depth. The notch depths for the 18- and 100-m source depths of the maximum profile tend to be closer, so the gain there is not as large. The advantage of a suspended array over a bottomed array is less than 2 dB for this profile at all ranges. For the minimum profile, the difference reaches 3 dB. Thus, for Site 3, the gain for different seasons is between 2 and 3 dB.

(U) In Fig 42 and 43, losses for Site 3 at 140 Hz are shown. Here we see the notch varying above the bottom from 5 to 10 m for the 18-m source and from 10 to 15 m for the 100-m source. Near 10 m good gains over a bottomed array can be obtained. Near 35 m off the bottom the beats are out of phase, and even larger gains (6 dB) can be obtained. However, within a few meters of this depth, the opposite effect will occur. The noise will be enhanced and the submarine signal weakened. It is apparent that utilizing the notch to gain signal-to-noise ratio will require careful planning because of differences due to frequency, site, and season.

ANALYSIS (U)

(U) The preceding figures show that a notch usually exists above the sea floor. In this section we will discuss the mechanism of the notch and use it to explain the best depth to utilize this notch.

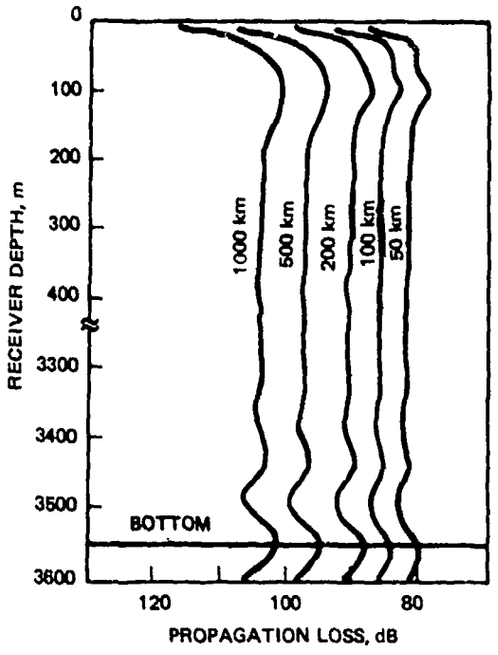

(UNCLASSIFIED)

(U) Figure 40. Propagation loss near the surface and bottom for a 100-m source depth for the Site 3 maximum profile, 25 Hz.

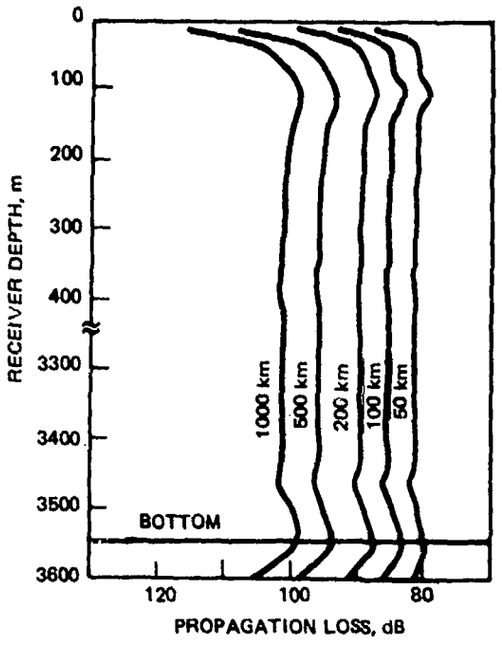

(UNCLASSIFIED)

(U) Figure 41. Propagation loss near the surface and bottom for a 100-m source depth for the Site 3 minimum profile, 25 Hz.

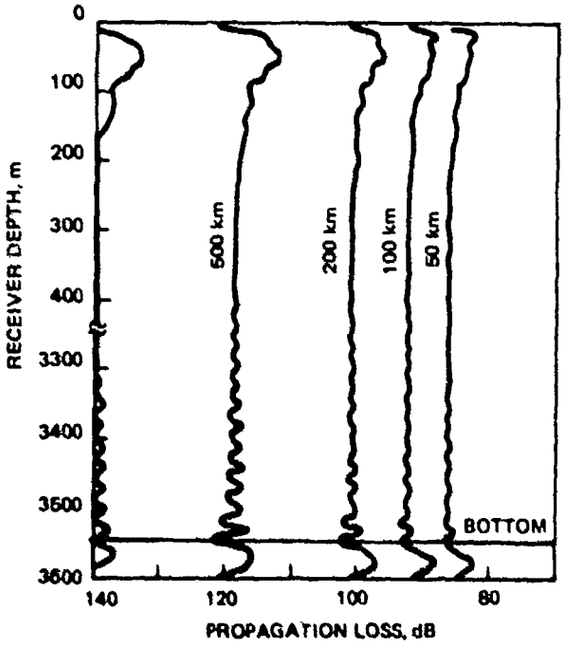

(UNCLASSIFIED)

(U) Figure 42. Propagation loss near the surface and bottom for an 18-m source depth, Site 3, 140 Hz.

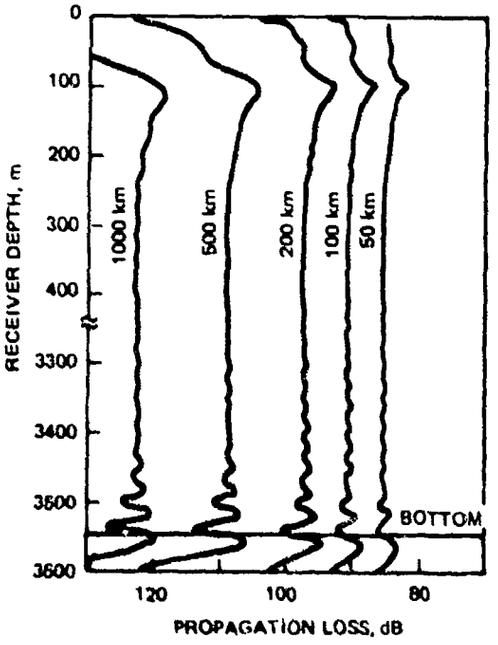

(UNCLASSIFIED)

(U) Figure 43. Propagation loss near the surface and bottom for a 100-m source depth, Site 3, 140 Hz.

(U) The pattern in propagation loss near the bottom arises from the sum of a number of modes. The change in the shape of the pattern as range increases is caused by higher order modes decreasing and disappearing due to their higher attenuation. They have higher attenuation because there is a general increase in bottom reflection loss with higher grazing angle (which corresponds to higher mode number), and also because the distance between bottom encounters becomes smaller with higher mode number.

(U) The sequence of modes that determines the loss at the bottom for a Site 3 25-Hz, 18-m source is shown in Fig 44 on a decibel loss scale. The upper set of points is the depth function response at the bottom for each mode. The two lower sets of points show the response of these modes at 100 and 1000 km range. The range spreading factor is omitted, being the same for each mode. Responses are plotted versus mode number and also bottom grazing angle of the equivalent ray. At 100 km range, the single strongest mode is number 53. At 1000 km range, the strongest mode is number 31. To gain an insight into the notch formation, we must now view this sequence for a receiver somewhat above the bottom.

(U) Figure 45 shows a similar mode sequence for a receiver 30m above the bottom. This is the location of the notch at 100 km range in Fig 32. In Fig 45, at 100 km range, mode 48 has the largest response. Furthermore, its response is about 2 dB below that of mode 53 in the previous figure. This roughly explains the increase in loss from the bottom to the notch depth in Fig 32.

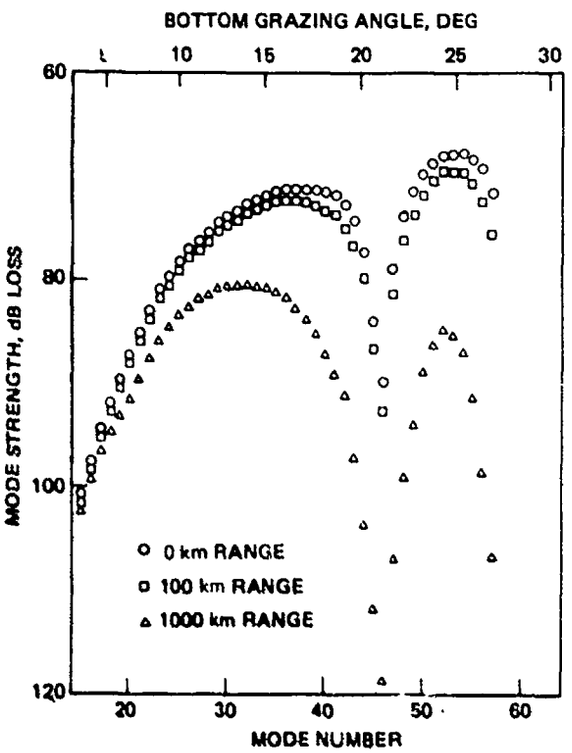

(UNCLASSIFIED)

(U) Figure 44. Strength of individual mode contributions to an 18-m source and 3555-m receiver (bottom) at Site 3, 25 Hz, for three different ranges. The range spreading factor, not included here, does not allow actual evaluation at zero range. The decibel scale is equivalent to loss.

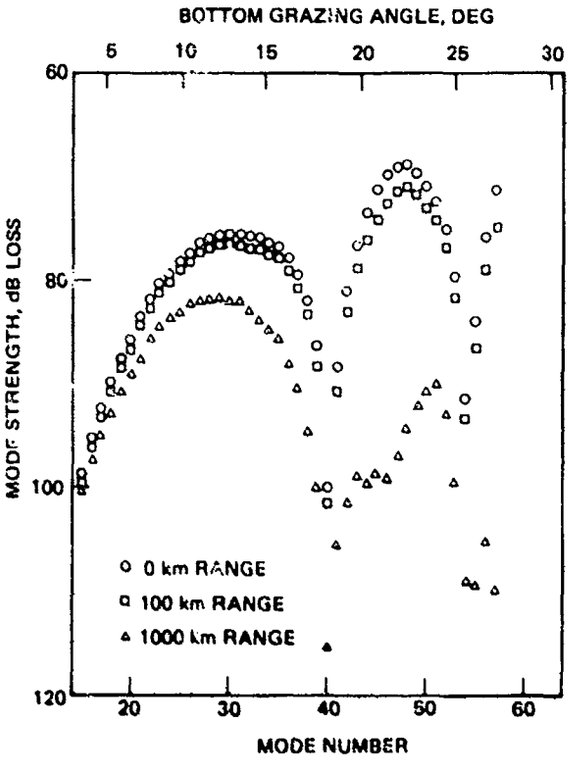

(UNCLASSIFIED)

(U) Figure 45. Strength of individual mode contributions to an 18-m source and 3525-m receiver (30m above bottom), Site 3, 25 Hz.

(U) These mode sequences can best be analyzed by showing the factors entering into them. These are the mode response at source, at receiver, and the mode attenuation. These are shown in Fig 46, 47, and 48. In Fig 46, the mode response at two source depths is shown. The 18-m source is the one used in the previous two figures. For this source depth, the modes are increasing in strength throughout this interval. This is because the source is close to the surface. The surface effect is discussed in a later section, "Near-Surface Sound Field." The equations there indicate that even the highest order modes, equivalent to almost vertical rays, cannot have nulls within one-half wavelength of the surface for the 18-m source depth. Therefore, no nulls will occur at the 18-m source, as is the case at the 100-m source near mode 44 in the figure. A maximum response should be reached at a grazing angle near 57 deg, which is off the scale of Fig 46.

(U) The shape of mode depth functions near the surface is predictable because the pressure-release effect requires that a null exist at the surface or, equivalently, that a phase shift of π radians occur upon surface reflection. The phase shift for bottom reflection is a function of grazing angle or mode number. The value of the mode depth functions at the bottom in Fig 47 corresponds to the phase shift there. At the nulls near modes 46 and 59, the reflection phase shift is π radians. Near the apexes of the curve, the phase shift is 0 deg, and the phase shift varies smoothly between these limits. For the receiver depths above the bottom, the pattern in Fig 47 shifts to the left. This can be seen by comparing Fig 44 and Fig 45.

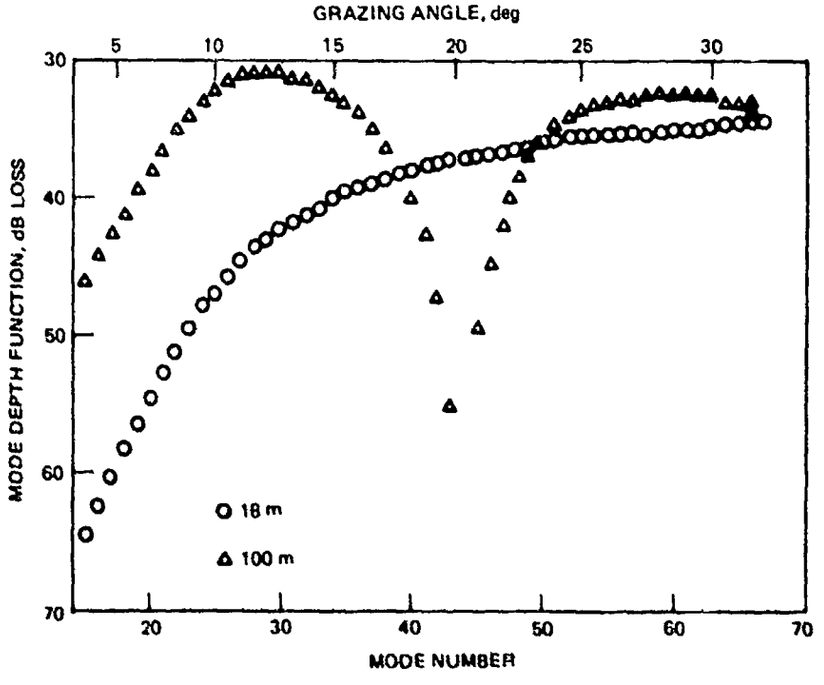

(UNCLASSIFIED)

(U) Figure 46. Magnitude of each mode depth function at two source depths, Site 3, 25 Hz.

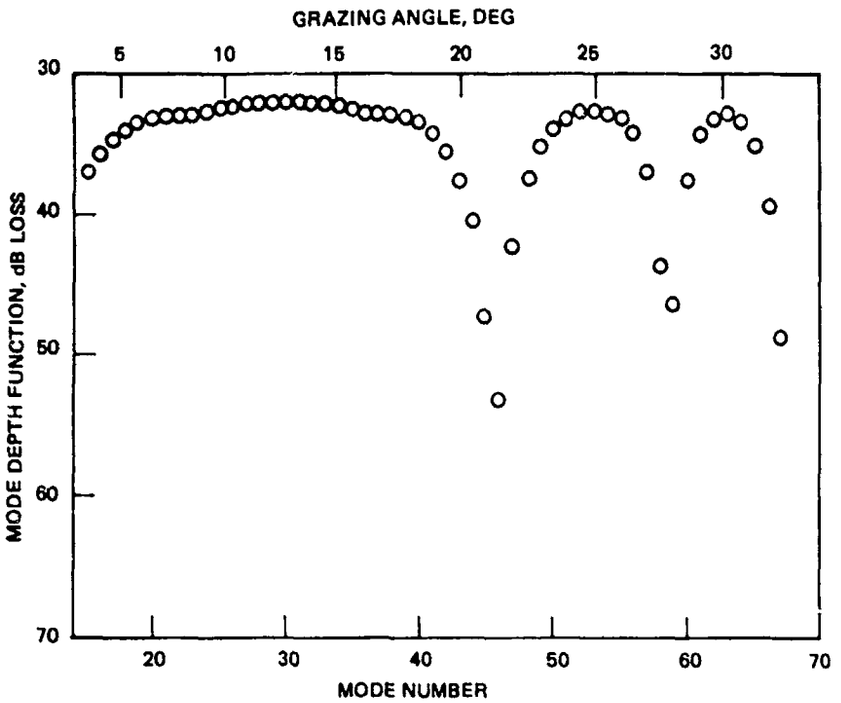

(UNCLASSIFIED)

(U) Figure 47. Magnitude of each mode depth function at the ocean bottom, Site 3, 25 Hz.

(U) Figure 48 shows the attenuation suffered by each mode at 1000 km range. The attenuation expressed in decibels is proportional to range. The sum of losses in Fig 46, 47, and 48 gives the losses shown in Fig 44 for 1000 km range.

(U) We can now explain the minimum in propagation loss at the ocean bottom as seen in figures such as Fig 32. At all ranges the loss increases towards a relative maximum at the notch as distance above the bottom increases. The loss is smallest at the bottom because the mode response and mode attenuation curves of Fig 47 and 48 are in optimum correlation at the bottom, that is, the modes with maximum depth function response are the modes with minimum attenuation loss. Modes with minimum depth function response, those in the nulls, also have greatest attenuation. As the receiver moves up from the bottom, the pattern in Fig 47 will change, but that for the attenuation in Fig 48 will remain the same. Now, the modes of maximum response will no longer be those of minimum attenuation.

(U) The surface effect also contributes to increased loss above the bottom. As the pattern in Fig 47 shifts to the left, increased loss at the 18-m source occurs, as shown in Fig 46. That is, as one moves up from the bottom, progressively lower order modes have maximum response, but lower order modes have a smaller response at the shallow source. Thus, shallow sources should lead to a pronounced notch with a clear decrease in loss from the notch to the bottom.

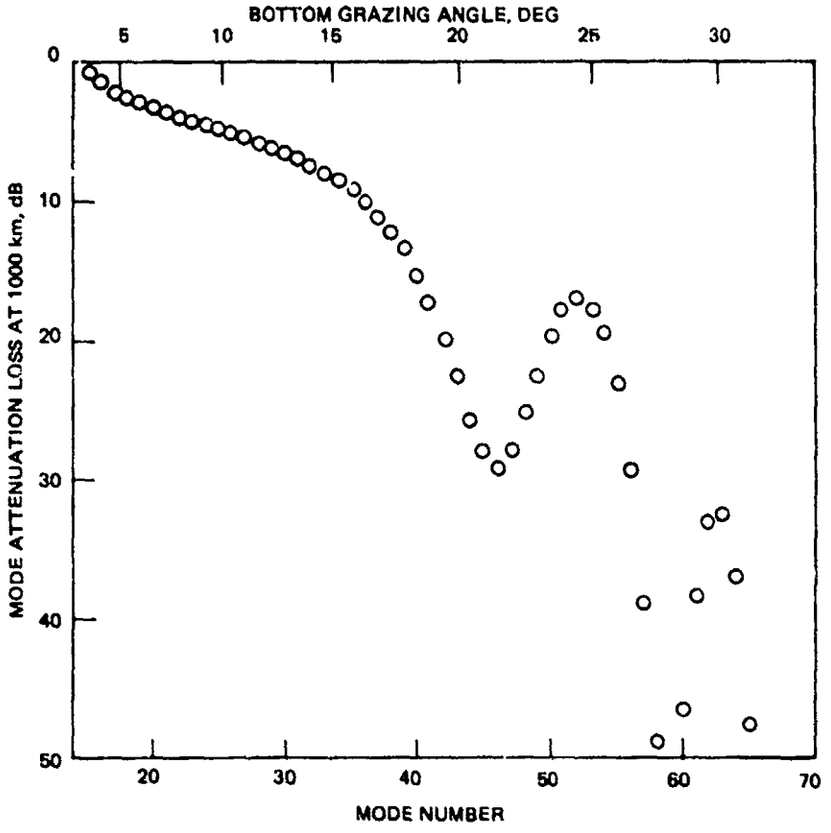

(UNCLASSIFIED)

(U) Figure 48. The loss through attenuation of each mode at 1000 km range for Site 3 at 25 Hz.

(U) The reason for the correlation between mode response and mode attenuation at the bottom can be seen in the phase of the reflection coefficient. Figure 49 shows the reflection loss and reflection phase shift as computed by normal modes for Site 3, 25 Hz. Note that as peaks of maximum loss occur, the phase passes through 180 deg. At minimums in loss, it passes through 0 deg. The mode attenuation is a function of the reflection loss, and the mode depth functions depend upon the phase shift. When a depth function has a maximum at the bottom, the attenuation is at a minimum. Therefore, the propagation loss has a minimum at the bottom.

(U) The preceding discussion can be illustrated by viewing the actual depth functions. Figure 50 shows the depth functions near the bottom for four modes. Mode 31 is the dominant mode at 1000 km range in Fig 44. The phase shift at the bottom is 6 deg, very near zero. Mode 46 has a phase shift of 172 deg at the bottom, very close to 180 deg. As can be seen, it has a very small response at the bottom. This mode is also at a local maximum in the attenuation curve of Fig 48. Mode 52 is the dominant mode at 100 km range. The bottom phase shift is 19 deg, again close to zero. Mode 37 is at a local maximum in Fig 44 and has a phase shift of −34 deg. At a receiver depth of 3525 m, the figure shows

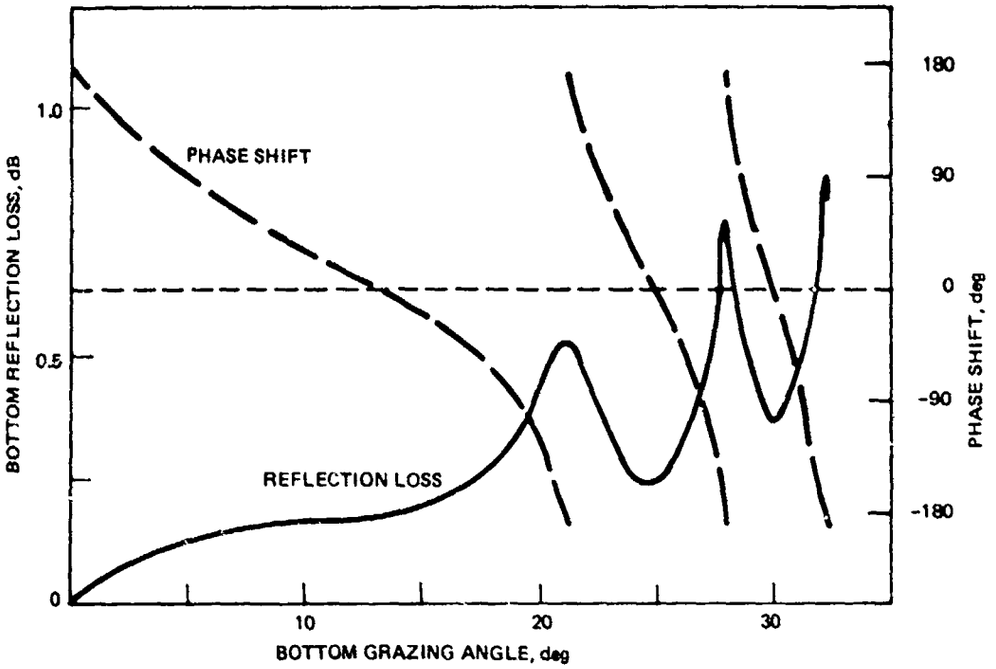

(UNCLASSIFIED)

(U) Figure 49. Reflection loss for Site 3, 25 Hz, with phase shift ϕ, the phase angle of the complex reflection coefficient.

that mode 46 has the greatest response of these four modes. Figure 45 shows that this is true at short ranges, but at 1000 km, the attenuation has greatly suppressed this mode. The mode response and attenuation are not correlated at this receiver depth for mode 46.

(U) The depths of minimum and maximum response of mode depth function can be estimated near the bottom. Appendix B shows that a half cycle, the depth difference, ΔZ, from one null to the next in these depth functions can be approximated by either

$$\Delta Z \approx \pi (C_b^3/2\,\omega^2 \Delta C)^{1/2}$$

or

$$\Delta Z \approx \pi\, C_b/\omega \sin \psi \qquad (9)$$

where C_b is the sound speed at the bottom, ω is the angular frequency, ψ is the grazing angle at the bottom, and ΔC is the difference between the phase velocity of the mode and C_b. Thus, ΔZ is inversely proportional to frequency and sin ψ or the square root of ΔC.

(U) As shown above, the position of the half cycle relative to the bottom depends upon the bottom reflection phase shift. The fraction F of ΔZ up to the first null is given by

$$F = (1/2 + \phi/360) \qquad (10)$$

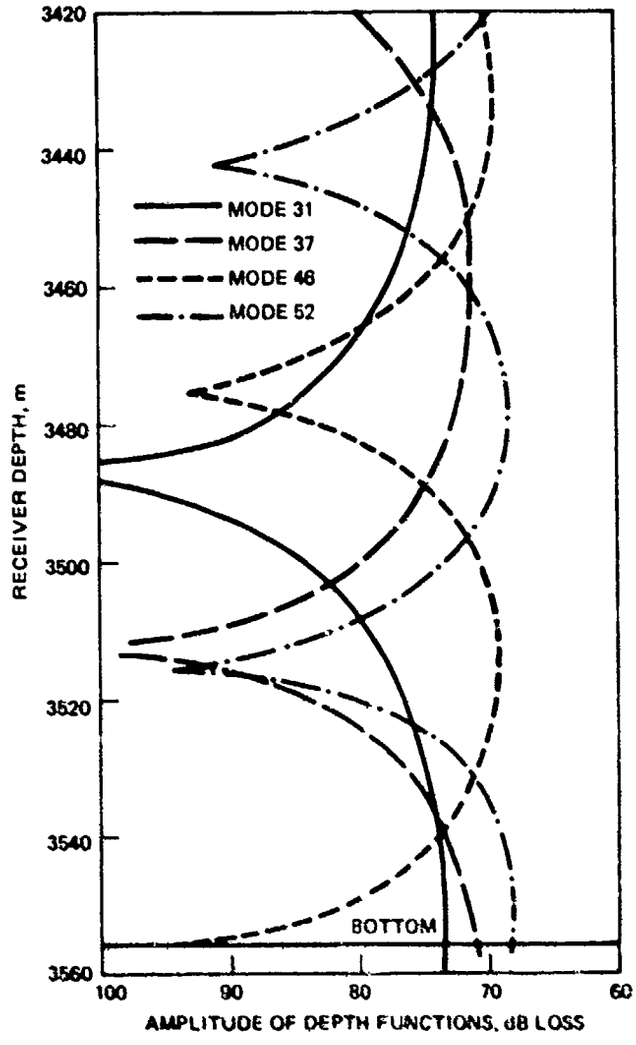

(UNCLASSIFIED)

(U) Figure 50. Magnitude of dimensionless depth functions for Site 3, 25 Hz, for an 18-m source depth. These four modes have bottom grazing angles of 13.4, 16.7, 21.4, and 24.5 deg.

where ϕ is the phase shift (in degrees) upon reflection. The maximums in the depth functions will be midway between the nulls. With Eq (9) and (10) and a plot of reflection phase shifts, one could estimate the shape of Fig 47 or a similar figure for receivers above the bottom.

(U) The curve of differences between 18- and 100-m source depths, Fig 34, must depend upon the difference in mode response at the two source depths of Fig 46. The differences in this figure are that the 18-m source depth curve increases monotonically. The 100-m curve is, for the stronger modes, decreasing from mode 28 on. The notch for the 18-m source depth occurs from 25 m above the bottom at 50 km range to 50 m at 1000 km range. The decorrelation depth above the bottom is one-quarter period or one-half of ΔZ in Eq (9) plus a correction for phase shift. This is the distance for a mode with maximum response at

the bottom to reach minimum response or a null. The 25 and 50m above correspond to modes with grazing angles of 37 and 18 deg plus some correction for phase shift. The dominant mode for the 100-m source in Fig 46 is at about 12 deg grazing angle, which has a decorrelation depth of 73m above the bottom, or 80m using ϕ of 18 deg in Eq (10). This depth corresponds to the depths of the minimums in Fig 34 or the depth at which the 100-m source has the fewest advantages over the 18-m source.

(U) Starting at the bottom and moving upward, the difference curves of Fig 34 increase because the 18-m source is reaching maximum decorrelation more rapidly than the 100-m source and also because the shallow source effect is added in. The decorrelation depth at 18m is range dependent, but above this depth the difference decreases rapidly to about 80m, where the minimum is reached as indicated above.

(U) An analysis of the notch effect at Site 1 is similar to that at Site 3, for the sediment parameters are similar and therefore the reflection losses are similar. Figure 51 shows reflection phase shifts for these two sites at two frequencies as computed by normal modes.

(U) Site 5 is more complicated and no analysis will be attempted. The increased complication arises from three factors. First, Site 5 is less severely bottom limited, and more modes at the low end of the bottom-reflected modes are admitted by the source. Second, reflection losses are lower, and more modes contribute from the higher end of the mode sequence. Third, the slow sediment sound speed and sediment sound channel cause large variations in bottom-reflection phase shift. Figure 22 showed reflection losses at six different frequencies. Figure 52 shows the corresponding phase shifts. The effect of such phase behavior on notches should be investigated at a future time.

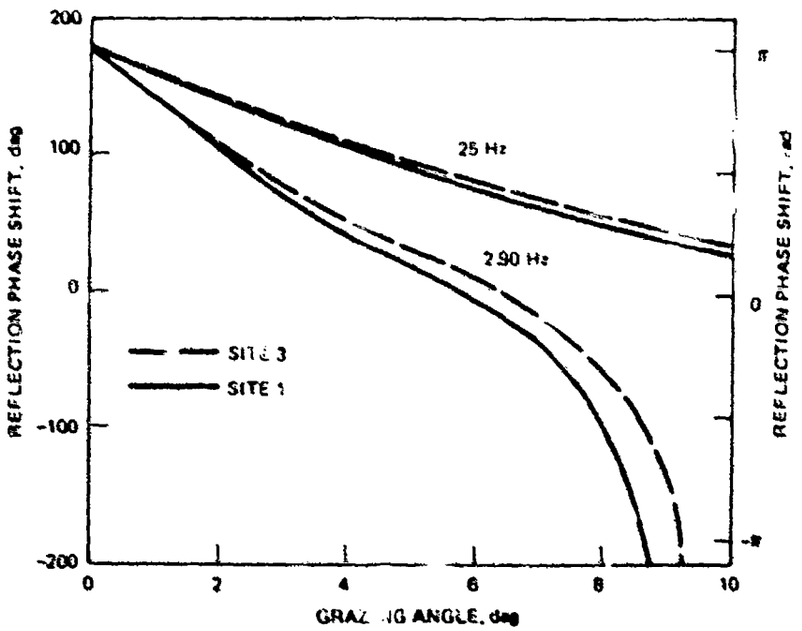

(UNCLASSIFIED)

(U) Figure 51. Reflection phase shift, ϕ, for Sites 1 and 3 at two frequencies.

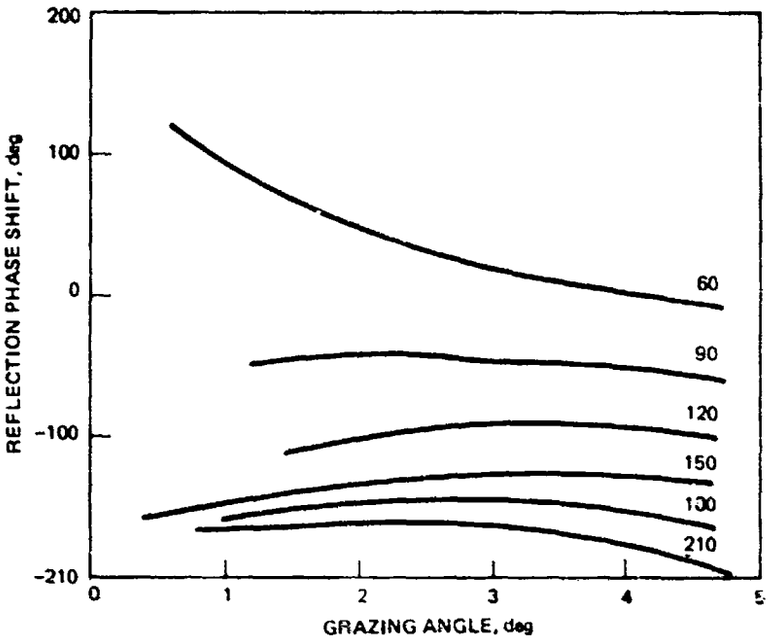

(UNCLASSIFIED)

(U) Figure 52. Reflection phase shift, ϕ, for Site 5 at six different frequencies

(U) At 25 Hz, the sediment sound channel has little effect, and Fig 53 shows the amplitude and phase of the reflection losses for Site 5. They are quite similar to those for Site 3.

NEAR-SURFACE SOUND FIELD (U)

(U) The preceding figures have shown near-surface propagation effects as well as near-bottom effects. The near-surface propagation is dominated by two effects, the surface decoupling effect and the minimum in loss when source and receiver are at the same depth. The 25-Hz losses generally show a relative minimum in loss at a receiver depth of 100 m when the source is at 100 m. When the source is at 18 m depth, this minimum is not seen because it is within the surface decoupling region, defined below. At 140 Hz, a relative minimum can be seen at the source depth in both cases, except at the longer ranges for the 18-m source in Fig 42. A similar minimum at the conjugate depth of the source does not occur at these sites because the bottom limiting prevents a conjugate depth in the water. The Site 5 minimum profile is an exception. Loss versus depth is not given here for it, but the upper curve in Fig 28 shows losses for a receiver near this conjugate depth of 3950 m.

(U) Surface decoupling is defined in Ref 9. It is the rapid decrease in acoustic pressure near the surface because of the pressure-release effect at the surface. It can also be thought of as a result of the 180-deg jump in acoustic phase upon reflection from the surface.

9. NUC Technical Paper 488, "Low-Frequency Propagation Effects for Sources or Receivers Near the Ocean Surface," M.A. Pedersen, D.F. Gordon, and D. White, Sept 1975.

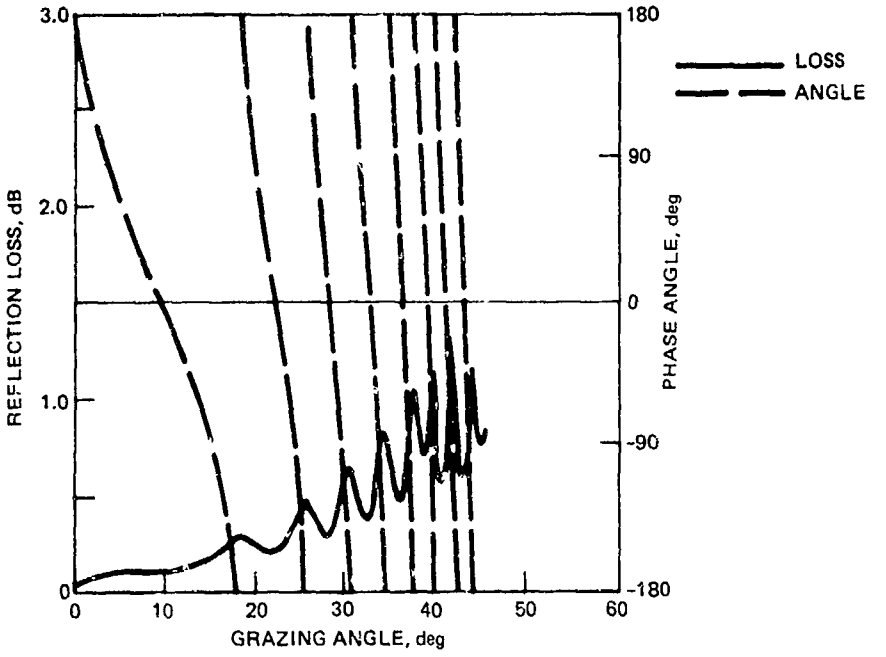

(UNCLASSIFIED)

(U) Figure 53. Reflection loss and phase shift for Site 5 at 25 Hz.

The definition mentioned above assumes that there is a maximum ray angle of propagation or maximum phase velocity. This occurs for surface-ducted propagation and for deep-water propagation if the bottom is lossy and represents an upper bound to propagating energy. The Bearing Stake sites are quite different. Because of the low bottom losses, sound propagates at large angles to the horizontal by bottom-reflected paths. There is no firm upper bound to ray angles here. This leads to surface decoupling effects quite different from those in Ref 8.

(U) The surface decoupling depth, Z_{SD}, for a single mode is the depth of the first minimum in propagation loss below the surface. Surface decoupling effects occur between this depth and the surface. Reference 8 shows that the surface decoupling depth can be approximated by

$$Z_{SD} = \lambda/4 \sin \theta \tag{11}$$

where λ is the acoustic wavelength, and θ is the angle the equivalent ray makes with the surface. Snell's law gives θ by

$$\cos \theta = C_o/C_m \tag{12}$$

where C_o is the sound speed at the surface and C_m is the phase velocity. If there were a limiting ray, C_m would be the phase velocity of that ray. The decoupling depth is just one-half of ΔZ in Eq (9).

(U) Figure 29 and subsequent figures show the surface decoupling depth increasing with range. This is because with increasing range, the high-angle rays are attenuated and sin θ in Eq (11) becomes smaller. The surface decoupling depth then becomes larger.

(U) Equation (11) should, in some sense, give the angle of the highest angle rays still propagating at each range. In Fig 32, for instance, the decoupling depth increases from 30 to 80 m. The angle θ therefore decreases from 31 to 11 deg between 50 and 1000 km range. Similar analysis for Site 1 gives 31 to 9 deg and for Site 5, 44 to 16 deg. At Site 3, 140 Hz, the decoupling depth increases from 18 to 50 m, giving maximum angles of propagation of 9 to 3 deg. These results agree with intuition. The lowest loss bottom, that of Site 5, supports the highest angle propagation at a given range. At the higher frequency, with greater bottom loss, the maximum angles of propagation are much smaller.

(U) The results of the last paragraph do not agree well with the analysis of the notch in the preceding section, which for Site 3 said the bottom grazing angles of strongest propagation varied from 37 to 18 deg. These correspond to surface grazing angles of 36 to 15 deg. This disagrees with highest angles still propagating -- 31 and 11 deg. The discrepancy arises from Fig 32, in which the surface decoupling depth is always a little larger than the distance from the notch to the bottom, yet we used the same formula, one-quarter of the period, to interpret results. The analysis of the bottom notch probably accounts for most of the error, because it is a more complex situation and the phase shift, ϕ, was ignored. The fairly close agreement between decoupling depth and notch depth suggests that they arise from similar mechanisms, though.

CONCLUSIONS (U)

(C) Propagation losses at the three bottom-limited Bearing Stake sites, 1, 3, and 5, are compared here with normal mode computations. Least squares fits to selected data in 50-km bins give a measure for overall level, H_0, and an attenuation, α, which is a function of bottom reflection loss. Conclusions are:

1. (C) H_0 at 25 Hz indicates that the source levels assumed for the towed projector are 1.5 to 2 dB too small. The actual source level was higher.

2. (C) At 140 and 290 Hz, there may be an even larger discrepancy between the actual projector output level and that used for analyzing the data. However, other factors such as larger attenuation may be the cause of this discrepancy.

3. (U) The attenuation α for data computed by normal modes is two to four times larger than for observed data. Bottom reflection loss is the main cause of attenuation.

4. (U) Reflection losses computed by normal modes using ARL sediment models are reasonably close to observed reflection losses. Therefore, observed reflection losses and observed propagation losses are not in agreement.

(U) Archived sound speed profiles with maximum and minimum sound speed at 100 m depth were selected for each site. Propagation losses were compared using these extreme profiles. Conclusions were:

1. At 25 Hz seasonal differences in propagation were less than 2 dB to 750 km range.

2. At 140 Hz seasonal propagation loss differences were equal to or less than 19 dB to ranges of 750 km.

3. The maximum and minimum profiles did not occur in any predictable season of the year.

(U) Average propagation loss was computed and plotted in the upper and lower 400 m of the ocean. Conclusions were:

1. Except near the upper and lower boundaries of the ocean, the average propagation loss is nearly constant with depth in these bottom-limited sites.

2. Average propagation loss usually has a relative minimum at the ocean bottom and increases to a relative maximum or notch just above the bottom. At 25 Hz, this notch is between 10 and 50 m above the bottom.

3. When target and noise sources are at different depths, a depth above the bottom can be chosen at which a receiver will have a better signal-to-noise ratio than a receiver on the bottom by up to 3 dB. This depth is frequency dependent. It is tens of meters above the bottom at 25 Hz.

4. A surface decoupling depth cannot be estimated by established formulas because there is no sharp cutoff to energy propagating at high angles. The surface decoupling depth increases with range.

REFERENCES (U)

1. NOSC Technical Report 467, "Propagation Loss Assessment of the Bearing Stake Exercise (U)," M.A. Pedersen and G.S. Yee, Sept 1979. (CONFIDENTIAL)
2. NOSC Technical Report 664, "Array Simulation at the Bearing Stake Sites (U)," April 1981. (CONFIDENTIAL)
3. NOSC Technical Report 393, "Underwater Sound Propagation Loss Program, Computation by Normal Modes for Layered Oceans and Sediments," D.F. Gordon, May 1979.
4. NORDA Report 18, "Bearing Stake Exercise: Sound Speed and Other Environmental Variability (U)," D.F. Fenner and W.J. Cronin, Jr., Sept 1978. (CONFIDENTIAL)
5. ARL-TR-79-24, "Analysis of Acoustic Bottom Interaction in Bearing Stake (U)," S.K. Mitchell and others, Feb 1979. (CONFIDENTIAL)
6. M.A. Pedersen, et al, "Comparison of Theoretical and Experimental Statistical Distributions of Bearing Stake Propagation Loss" (NOSC TR in preparation).
7. W.H. Thorp, "Analytic Description of the Low-Frequency Attenuation Coefficient," J. Acoust. Soc. Am., 42:1, p 270, July 1967.
8. NUC Technical Paper 502, "Sound-Speed Distribution in the Western Indian Ocean," J.G. Colborn, Feb 1976.
9. NUC Technical Paper 488, "Low-Frequency Propagation Effects for Sources or Receivers Near the Ocean Surface," M.A. Pedersen, D.F. Gordon, and D. White, Sept 1975.

APPENDIX A: SEDIMENT ACOUSTIC DUCTS (U)

(U) A slow bottom, that is, sediment sound speed less than the water sound speed, creates a duct in the sediment. This duct is bounded by the water of higher sound speed at the top and the steep positive sound speed gradient below. The Site 5 sediment model is of this type, and in this appendix we will show some consequences of this sediment duct.

(U) This duct was first noticed when it caused failures of a usually reliable method of finding eigenvalues. This method is simply to estimate the eigenvalue by extrapolation from the three previous eigenvalues and then correct this estimate with a Newton-Rafson root finder. This extrapolation works well if a parabola can fit four consecutive eigenvalues closely. The sediment duct causes irregularities in the mode sequence, and modes there are not fit well by a parabola. This can be seen from the interference length between modes.

(U) The interference length between adjacent modes, the range interval required for one mode to gain a full phase cycle on another, is given by

$$L = 2\pi/\Delta k$$

where L is the interference length and Δk is the difference in the real part of the wave number between two modes. When computed between adjacent modes, this quantity gives the range interval between interference beats. Figure A-1 shows this distance for four frequencies for modes with phase velocities near the bottom sound speed. These modes are for the Site 5 maximum profile. The large peak at 140 Hz means the modes are not evenly spaced, and extrapolation from mode to mode is not a good estimate for the next mode.

(U) Modes can be related to rays with the same phase velocity. The scale at the top of Fig A-1 shows the distance above the bottom at which a corresponding ray will vertex or, if it reaches the bottom, the grazing angle at which it will contact the bottom. From this scale it can be seen that the unusual behavior in the modes takes place before they, in effect, reach the bottom.

(U) The interference length between modes can be equated with the loop length of the corresponding ray if the two modes are associated with the same duct. Figure A-1 therefore seems to indicate that some rays passing near the bottom have unusually long loop lengths. This may indicate that wave effects tend to curve the ray towards the bottom and cancel some of the normal upward curvature. However, the existence of a sediment duct may mean that adjacent modes are not associated with the same duct and that the usual ray – mode relationships cannot be used. Therefore, we will not pursue this explanation further. Coupling between the two ducts is a more accessible explanation.

(U) The sediment has an absorption loss (0.6 dB/km at 140 Hz), so modes that stimulate propagation in this duct will lose energy in the sediment. Figure A-2 shows the attenuation of near-bottom modes such as were shown in Fig A-1. It is apparent that some resonance condition is met near 140 Hz. It is presumably a coupling between a water mode and the first mode in the sediment. The mode depth functions support this supposition.

(U) Figure A-3 shows depth functions for several modes from the Site 5 minimum profile. The depth function labeled -7, the seventh mode preceding the first bottom-touching mode, is the mode of greatest attenuation. The sediment sound speed equals the phase velocity of this mode about 19 m below the sediment surface. The maximum in the depth function occurs 5 m below the sediment surface.

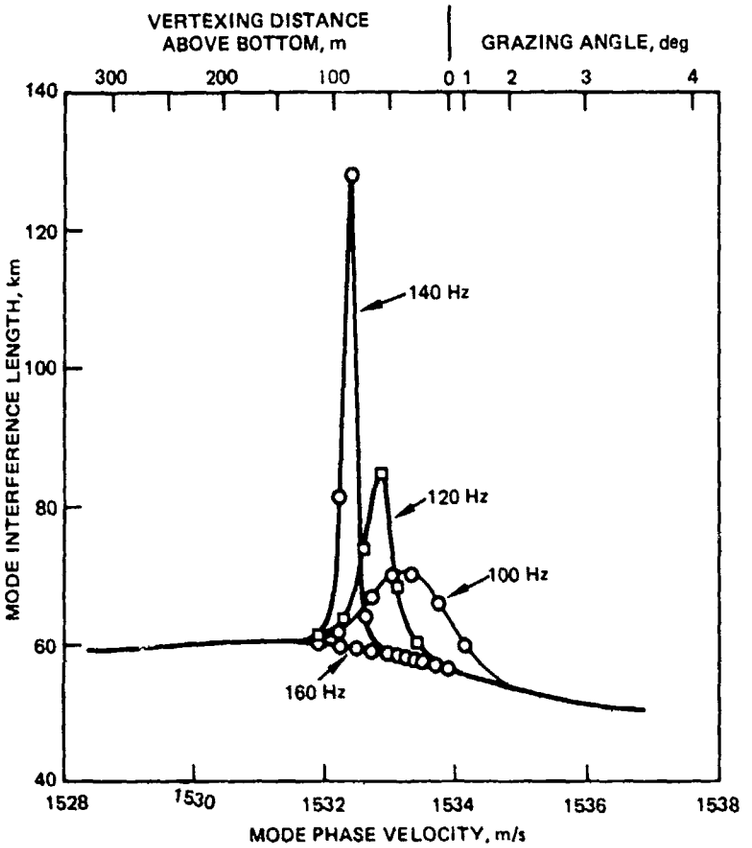

(UNCLASSIFIED)

(U) Figure A-1. Interference distance between modes for modes just preceding and following the first bottom grazing mode for Site 5. The upper scale refers to parameters for rays with the same phase velocities as the modes.

(U) Within the normal mode program, the identity of a mode can be determined from the change in a unitless depth parameter, $\zeta(z)$, through that part of a duct occupied by a mode -- the 19 m of the previous paragraph. A pressure-release surface with a phase angle of 180 deg requires a change in ζ of 2.33 to support mode 1. A rigid surface with 0 phase shift requires a change in ζ of 1.1. The changes in ζ for five consecutive modes with the mode of greatest loss in Fig A-2 in the center are 1.32, 1.35, 1.36, 1.37, and 1.40. The corresponding phase shifts in the reflection coefficients from the underside of the sediment surface are -7.3, -10.0, -9.3, -18.3 and -123.3 deg. These numbers do not exclude the existence of a mode in the bottom in any of the five cases. On the other hand, they do not add any confidence to the explanation of the mode structure. Over this sequence of five modes, the depth of the maximum of the depth function in the sediment increases by 2 m. It appears that these modes are being driven by the much more extensive modes in the water above, and the maximum effect at the middle mode is evidence of optimum coupling. Previous experience indicates that this should happen when the phase velocity of a mode in the water happens to be very close to the phase velocity of a mode in the sediment.

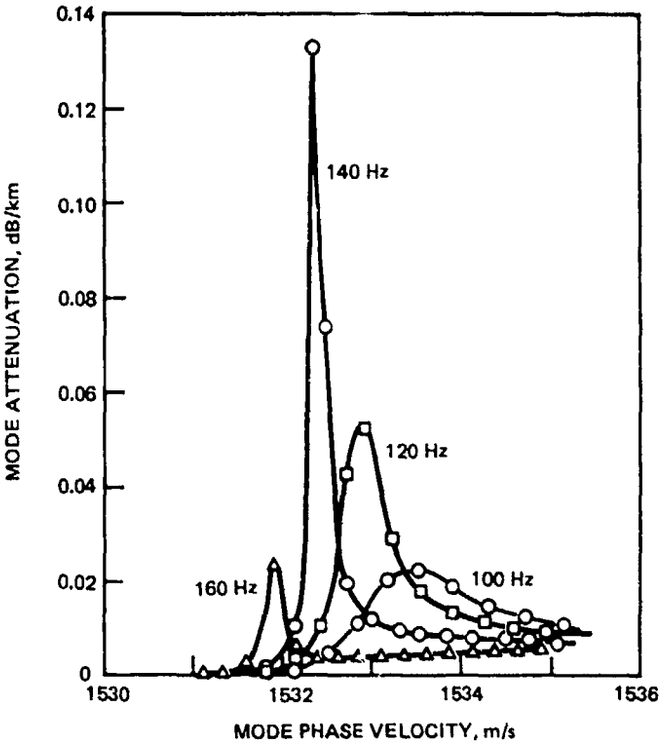

(UNCLASSIFIED)

(U) Figure A-2. Attenuation of modes for Site 5.

However, the regular sequence in maximums in Fig A-2 indicates some more precise relationship that we have not discovered.

(U) In one further study we changed the jump in sound speed between water and sediment to only 75 percent of the given value. We obtained a similar peaking in mode attenuation, now around 210 Hz rather than 140 Hz. At this mode, the change in ζ was again 1.36.

(U) Modes such as these will cause better than normal propagation to near-bottom receivers (or sources) at relatively short ranges. However, their high attenuation will damp out their effect at longer ranges. The damping will equal the excess response in about 100 km. Therefore, some near-bottom enhancement should be observable to ranges of less than 100 km.

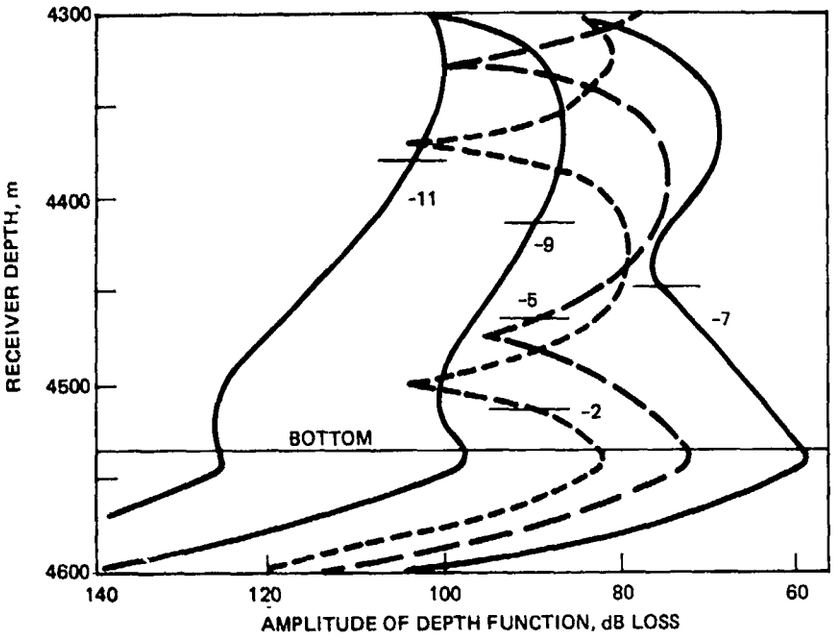

(UNCLASSIFIED)

(U) Figure A-3. Amplitude of mode depth functions for Site 5 minimum profile at 140 Hz. Source depth is 4534 m (bottom depth). Modes are numbered relative to the first bottom mode. Vertexing depths of corresponding rays are marked.

APPENDIX B: MODE DEPTH FUNCTIONS NEAR THE BOTTOM (U)

(U) The height above the bottom of a cycle in the depth function for a given mode can be estimated. To find the depth interval from null to null or peak to peak, we look for a half-cycle or π change in phase of the depth function. The depth function is essentially an Airy function of the unitless depth parameter ζ (Z) given by

$$\zeta(Z) = \left[a^3 (Z - Z_b) + \omega^2 \left(1/C_b^2 - 1/C_p^2\right)\right] a_i^2 \qquad \text{(B-1)}$$

where

$$a^3 = -2 \gamma_i \omega^2 / C_b^3$$

and Z is depth, Z_b is the bottom depth, C_b is the water bottom sound speed, C_p is the phase velocity of the mode, ω is the angular frequency, and γ_i is the sound speed gradient. The depth function may be an Airy function with shifted phase, but here we are looking for a phase difference of one-half period, so the shifted phase does not matter. The first term of the asymptotic series for the phase of an Airy function is given by

$$\theta(-\zeta) - \pi/4 \approx \frac{2 \zeta^{3/2}}{3} \quad . \qquad \text{(B-2)}$$

Assuming the second term in the square brackets of Eq (B-1) is large compared to the first two terms of a binomial expansion of $\zeta^{3/2}$, then

$$\zeta^{3/2} \approx \left[\omega^2 \left(1/C_b^2 - 1/C_p^2\right)/a^2\right]^{3/2} + 3a (Z - Z_b) \omega \left(1/C_b^2 - 1/C_p^2\right)^{1/2}/2a \, . \qquad \text{(B-3)}$$

Taking the difference in $\theta(-\zeta)$ at two values of Z gives

$$\theta(-\zeta_1) - \theta(-\zeta_2) = (Z_1 - Z_2) \omega \left(1/C_b^2 - 1/C_p^2\right)^{1/2} \quad . \qquad \text{(B-4)}$$

Letting this phase change be π and approximating C_p with C_b but keeping their difference, ΔC, we obtain

$$\Delta Z \approx \pi \left(C_b^3/2 \, \omega^2 \Delta C\right)^{1/2} \quad . \qquad \text{(B-5)}$$

The quantity ΔZ approximates the distance between nulls in the depth function. We see this depth interval is inversely proportional to the square root of ΔC and to the frequency.

(U) By Snell's law, the grazing angle ψ at the bottom is given by

$$\sin \psi = C_b \left(1/C_b^2 - 1/C_p^2\right)^{1/2} \quad . \qquad \text{(B-6)}$$

Using this in Eq (B-4) gives an alternate expression for ΔZ:

$$\Delta Z = \pi C_b / \omega \sin \psi \, . \qquad \text{(B-7)}$$

(U) Equation (B-2) is reliable to two places for ΔC greater than 2 m/s, or about 3 deg grazing angle. Approximations going from Eq (B-2) to (B-3) and from (B-4) to (B-5) should have two-place accuracy for grazing angles below 15 deg. The above analysis is most accurate for real eigenvalues. Eigenvalues with appreciable imaginary parts, meaning lossy modes, will give less accuracy in Eq (B-5) and (B-7).

DEPARTMENT OF THE NAVY
OFFICE OF NAVAL RESEARCH
875 NORTH RANDOLPH STREET
SUITE 1425
ARLINGTON VA 22203-1995

IN REPLY REFER TO:

5510/1
Ser 321OA/011/06
31 Jan 06

MEMORANDUM FOR DISTRIBUTION LIST

Subj: DECLASSIFICATION OF LONG RANGE ACOUSTIC PROPAGATION PROJECT (LRAPP) DOCUMENTS

Ref: (a) SECNAVINST 5510.36

Encl: (1) List of DECLASSIFIED LRAPP Documents

1. In accordance with reference (a), a declassification review has been conducted on a number of classified LRAPP documents.

2. The LRAPP documents listed in enclosure (1) have been downgraded to UNCLASSIFIED and have been approved for public release. These documents should be remarked as follows:

   Classification changed to UNCLASSIFIED by authority of the Chief of Naval Operations (N772) letter N772A/6U875630, 20 January 2006.

   DISTRIBUTION STATEMENT A: Approved for Public Release; Distribution is unlimited.

3. Questions may be directed to the undersigned on (703) 696-4619, DSN 426-4619.

BRIAN LINK
By direction

Subj: DECLASSIFICATION OF LONG RANGE ACOUSTIC PROPAGATION PROJECT (LRAPP) DOCUMENTS

DISTRIBUTION LIST:

NAVOCEANO (Code N121LC – Jaime Ratliff)
NRL Washington (Code 5596.3 – Mary Templeman)
PEO LMW Det San Diego (PMS 181)
DTIC-OCQ (Larry Downing)
ARL, U of Texas
Blue Sea Corporation (Dr.Roy Gaul)
ONR 32B (CAPT Paul Stewart)
ONR 321OA (Dr. Ellen Livingston)
APL, U of Washington
APL, Johns Hopkins University
ARL, Penn State University
MPL of Scripps Institution of Oceanography
WHOI
NAVSEA
NAVAIR
NUWC
SAIC

Declassified LRAPP Documents

Report Number	Personal Author	Title	Publication Source (Originator)	Pub. Date	Current Availability	Class.
ARLTR7952	Focke, K. C., et al.	CHURCH STROKE 2 CRUISE 5 PAR/ACODAC ENVIRONMENTAL ACOUSTIC MEASUREMENTS AND ANALYSIS (U)	University of Texas, Applied Research Laboratories	791029	ADC025102; NS; AU; ND	C
Unavailable	Van Wyckhouse, R. J.	SYNBAPS. VOLUME I. DATA BASE SOURCES AND DATA PREPARATION	Naval Ocean R&D Activity	791201	ADC025193	C
NORDATN63	Brunson, B. A., et al.	ENVIRONMENTAL EFFECTS ON LOW FREQUENCY TRANSMISSION LOSS IN THE GULF OF MEXICO (U)	Naval Ocean R&D Activity	800901	ADC029543; ND	C
NORDATN80C	Gereben, I. B.	ACOUSTIC SIGNAL CHARACTERISTICS MEASURED WITH THE LAMBDA III DURING CHURCH STROKE III (U)	Naval Ocean R&D Activity	800915	ADC023527; NS; AU; ND	C
NOSCTR664	Gordon, D. F.	ARRAY SIMULATION AT THE BEARING STAKE SITES	Naval Ocean Systems Center	810401	ADC025992; NS; AU; ND	C
NOSCTR703	Gordon, D. F.	NORMAL MODE ANALYSIS OF PROPAGATION LOSS AT THE BEARING STAKE SITES (U)	Naval Ocean Systems Center	810801	ADC026872; NS; AU; ND	C
NOSCTR680	Neubert, J. A.	COHERENCE VARIABILITY OF ARRAYS DURING BEARING STAKE (U)	Naval Ocean Systems Center	810801	ADC028075; NS; ND	C
HSECO735	Luehrmann, W. H.	SQUARE DEAL R/V SEISMIC EXPLORER FIELD OPERATIONS REPORT (U)	Seismic Engineering Co.	731121	AD0530744; NS; ND	C; U
MPL-C-42/76	Morris, G. B.	CHURCH ANCHOR EXPLOSIVE SOURCE (SUS) PROPAGATION MEASUREMENTS FROM R/P FLIP (U)	Marine Physical Laboratory	760701	ADC010072; AU; ND	C; U
ARLTR7637	Mitchell, S. K., et al.	SQUARE DEAL EXPLOSIVE SOURCE (SUS) PROPAGATION MEASUREMENTS. (U)	University of Texas, Applied Research Laboratories	760719	ADC014196; NS; AU; ND	C; U
NORDAR23	Fenner, D. F.	SOUND SPEED STRUCTURE OF THE NORTHEAST ATLANTIC OCEAN IN SUMMER 1973 DURING THE	Naval Ocean R&D Activity	800301	ADC029546; NS; ND	C; U
NOOTR230	Bucca, P. J.	SOUND VELOCITY CONDITIONS DURING THE CHURCH ANCHOR EXERCISE (U)	Naval Oceanographic Office	751201	NS; AU; ND	C;U
ONR SP 2-69; MC PLAN-01	Unavailable	PARKA II EXPERIMENT UTILIZING SEA SPIDER, ONR SCIENTIFIC PLAN 2-69 (U)	Maury Center for Ocean Science	690626	ADB020846; ND	U
Unavailable	Unavailable	PARKA I EXPERIMENT	Maury Center for Ocean Science	691101	AD0506209	U
USRD CR 3105	Unavailable	SEA SPIDER TRANSPONDER TRANSDUCER	Naval Research Laboratory	700505	ND	U
MC PLAN 05; ONR Scientific Plan 1-71	Unavailable	ATLANTIC TEST BED MEASUREMENT PROGRAM (U)	Maury Center for Ocean Science	701020	ND	U
ACR-170 VOL.1	Hurdle, B. G.	PROJECT NEAT- A COLLABORATIVE LONG RANGE PROPAGATION EXPERIMENT IN THE NORTHEAST ATLANTIC, PART I (U)	Naval Research Laboratory	701118	ND	U
MC-003-VOL-2	Unavailable	THE PARKA I EXPERIMENT. APPENDICES- PACIFIC ACOUSTIC RESEARCH KANEOHE-ALASKA (U)	Maury Center for Ocean Science	710101	ND	U